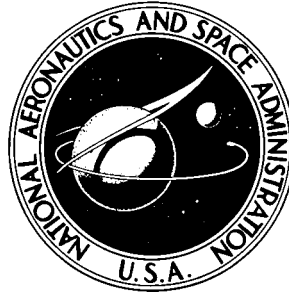


**NASA TECHNICAL NOTE**



*N73-20915*  
NASA TN D-7243

NASA TN D-7243

**CASE FILE  
COPY**

# **THERMAL STATIC BENDING OF DEPLOYABLE INTERLOCKED BOOMS**

*by Charles L. Staugaitis and Roamer E. Predmore*

*Goddard Space Flight Center*

*Greenbelt, Md. 20771*

1. Report No. NASA TN D-7243	2. Government Accession No.	3. Recipient's Catalog No.	
4. Title and Subtitle Thermal Static Bending of Deployable Interlocked Booms		5. Report Date March 1973	
		6. Performing Organization Code	
7. Author(s) Charles L. Staugaitis and Roamer E. Predmore		8. Performing Organization Report No. G-1076	
9. Performing Organization Name and Address  Goddard Space Flight Center Greenbelt, Maryland 20771		10. Work Unit No.	
		11. Contract or Grant No.	
		13. Type of Report and Period Covered  Technical Note	
12. Sponsoring Agency Name and Address  National Aeronautics and Space Administration Washington, D.C. 20546		14. Sponsoring Agency Code	
15. Supplementary Notes			
16. Abstract  Metal ribbons processed with a heat-forming treatment are enabled to form tubelike structures when deployed from a roll. Deployable booms of this kind have been utilized for gravity-gradient stabilization on the RAE, ATS, and Nimbus D satellites. An experimental thermal-mechanics test apparatus was developed to measure the thermal static bending and twist of booms up to 3 m long. The apparatus was calibrated by using the correlation between calculated and observed thermal bending of a seamless tube. Thermal static bending values of 16 interlocked deployable booms were observed to be within a factor of 2 of the values calculated from seamless-tube theory. Out-of-Sun-plane thermal bending was caused by complex heat transfer across the interlocked seam. Significant thermal static twisting was not observed.			
17. Key Words (Selected by Author(s)) Gravity gradient booms Deployable boom structures Thermal-mechanics test facility		18. Distribution Statement  Unclassified—Unlimited	
19. Security Classif. (of this report) Unclassified	20. Security Classif. (of this page) Unclassified	21. No. of Pages 47	22. Price* \$3.00

\*For sale by the National Technical Information Service, Springfield, Virginia 22151.

## FOREWORD

In accordance with the policy of the National Aeronautics and Space Administration, this document employs the international system of units, designated SI units. Certain data are expressed in English units as well for improved communication and because they were determined in that system. The non-SI units, given in parentheses following their computed SI equivalents, are the basis of the measurements and calculations reported here, except for boomtip deflection measurements.

## CONTENTS

	<i>Page</i>
ABSTRACT . . . . .	i
FOREWORD . . . . .	iii
INTRODUCTION . . . . .	1
TEST PROCEDURE . . . . .	2
Thermal-Mechanics Test Facility . . . . .	2
Theory of Thermal Bending for a Thin-Walled Cylinder . . . . .	5
Transient Thermal Bending . . . . .	6
Calculated Thermal Bending of a Perforated Seamless Tube . . . . .	8
Calibration of Measurements: Bending of a Black Seamless Tube . . . . .	9
Thermal Bending of a Be-Cu Seamless Tube . . . . .	13
Gravity Loading of a Thermally Bent Tube . . . . .	13
EXPERIMENTAL RESULTS FOR VARIOUS BOOM TYPES . . . . .	14
Be-Cu Interlocked (Westinghouse) . . . . .	15
Ag-Plated Be-Cu Interlocked (Fairchild-Hiller) . . . . .	15
Ag-Plated Be-Cu Hingelock (Fairchild-Hiller) . . . . .	17
Be-Cu Interlocked (Fairchild-Hiller) . . . . .	18
Ag-Plated Be-Cu Interlocked BI-STEM (SPAR), ½ in. . . . .	18
Ag-Plated Be-Cu Interlocked BI-STEM (SPAR), ¼ in. . . . .	21
Be-Cu Perforated, Interlocked (Westinghouse) . . . . .	21
Al-Black-Coated, Perforated, Interlocked (Westinghouse) . . . . .	21
Al-Black-Coated, Perforated, Interlocked, Low Pretwist (Westinghouse) . . . . .	21
Al-Black-Coated, Perforated, Interlocked Riveted Seam (Westinghouse) . . . . .	26
Ag-Black-Coated, Perforated, Interlocked (Fairchild-Hiller) . . . . .	26
Ag-Black-Coated, Perforated, Interlocked BI-STEM (SPAR) . . . . .	26
Overlapped, Rigidized Wire Screen (General Dynamics/Convair) . . . . .	35
THERMAL STATIC BENDING AND EFFECTIVE TEMPERATURE GRADIENT . . . . .	35
CONCLUSIONS . . . . .	39

**CONTENTS—concluded**

	<i>Page</i>
ACKNOWLEDGMENTS . . . . .	40
Appendix—TEST BOOM PROPERTIES, BENDING MEASUREMENTS, AND ABSORPTIVITIES . . . . .	41
REFERENCES . . . . .	47

# THERMAL STATIC BENDING OF DEPLOYABLE INTERLOCKED BOOMS

Charles L. Staugaitis and Roamer E. Predmore  
*Goddard Space Flight Center*

## INTRODUCTION

In a variety of space applications such as gravity-gradient passive stabilization, rollout solar arrays, support structures for instrument probes, and antennas, the use of deployable tubular elements is highly desirable or mandatory where volume and weight constraints are critical to spacecraft design.

The manufacture of these elements involves a variety of processing techniques, but essentially, all operations can be reduced to application of a forming treatment to a flat metal ribbon that enables it to form a tubelike structure when deployed from a flat spool. Depending on the particular requirement, the configurations can range from a simple unplated, overlapped Be-Cu boom to a complex configuration exhibiting interlocking seams, perforations, and, if necessary, highly reflective surface coatings. Deployable booms can be produced from metallic or nonmetallic materials in various sizes and length-to-diameter ( $L/D$ ) ratios commensurate with the need for maintaining structural integrity. A sampling of those GSFC spacecraft utilizing deployable booms includes the Radio Astronomy Explorer (RAE), Applications Technology Satellites (ATS's), Interplanetary Monitoring Platform (IMP), Nimbus, and Orbiting Geophysical Observatory (OGO).

The application of overlapped booms of open cross section for satellites was first presented by Warren and MacNaughton (ref. 1); later, the thermal-mechanical behavior was described by Frisch (ref. 2). With the advent of advanced configurations incorporating a variety of interlocking schemes, perforation patterns, and fabrication practices, modifications must be introduced into existing theoretical models to allow more rigorous prediction of thermoelastic-dynamic response in service. However, theoretical treatment of these complex concepts is not enough. Experimental verification must be obtained not only to insure the absence of any anomalous behavior but to permit assessing the degree of correlation with theory. As a consequence of previous research on boom materials, a unique thermal vacuum chamber facility was constructed for the thermal-mechanical evaluations of all boom concepts that either have flown or are intended for future flight. To minimize gravity-induced effects, this investigation necessarily restricted test specimen lengths to 3.0 m (10 ft), with corresponding  $L/D$  ratios ranging from approximately 60 to 240. Thermal response for the actual boom length could then be determined by extrapolation from the subsize-boom data, using the analysis for a seamless tube.

This report covers primarily the performance of three interlocking-boom concepts representing configurations currently receiving the most attention from spacecraft designers. These boom designs, described in appendix A, table A-1, represent developments by the Westinghouse Electric Corp.,

Baltimore, Md.; Fairchild-Hiller Corp., Germantown, Md.; SPAR Aerospace Products, Ltd., Toronto, Ontario; Convair Div., General Dynamics Corp., San Diego, Calif.; and a seam design by General Electric Co., Valley Forge, Pa.

## TEST PROCEDURE

The thermal-bending measurement procedure is based on the correlation between exact seamless-tube theory and observed seamless-tube bending.

### Thermal-Mechanics Test Facility

The thermal test chamber designed to evaluate the thermal bending plus twist of 3.0-m (10-ft) tubular elements is shown in figure 1. Essentially, it is a 4.3-m (14-ft) vertical cylinder of 0.46-m (18-in.) diameter incorporating a liquid-nitrogen-cooled shroud (blackened on the inside) maintained at an operating temperature below 90 K (-300° F). The high-speed, low-backstreaming pumping system is capable of achieving a pressure of  $10^{-5}$  N m<sup>-2</sup> ( $10^{-7}$  torr) or better.

The test booms are irradiated by means of a solar simulator consisting of forty-two 120-V, T3 tungsten-iodine lamps, sufficient to provide uniform illumination through a segmented 5-cm (2-in.) by 3.7-m (12-ft) quartz window in the chamber door. Each lamp is mounted in a water-cooled, multi-faceted paraboloid reflector and collimator. The front of the chamber is cooled by means of a forced air blower mounted below the solar-simulator housing to prevent excessive temperature buildup in the collimator assemblies.

The test booms are clamped at the top onto a support rod machined from invar (a low-thermal-expansion alloy), thus eliminating the clamping fixture as a possible source of bending error.

A motor drive mechanism provides a means for rotating the test booms, while a control panel indicator monitors its orientation with respect to the plane of incident radiation as shown in the cut-away drawing (fig. 2). An Eppley Mk I thermopile radiometer is used to calibrate solar-simulator intensity and insure uniformity of the source (ref. 3). This instrument is checked against a standard radiometer calibrated by the National Bureau of Standards (NBS). The spectral distribution (intensity versus wavelength) of the T3 lamp-reflector-quartz systems was measured at GSFC (ref. 4) using a spectrophotometer and a 1000-W tungsten-iodine lamp, also calibrated by the NBS. Results are shown in figure 3 with the solar spectrum. The heat flux of the simulator was obtained by moving the radiometer vertically along the chamber axis and recording the observed intensity at each lamp position. In 14 months of chamber operations, no significant degradation of the source was noted, with all but two lamps exhibiting a flux within  $\pm 5$  percent of the originally measured level of 138 mW cm<sup>-2</sup>.

The magnitude of static bending determined experimentally is influenced by such factors as thermal distortion of the chamber itself, stiffness and thermal response of the supporting mandrel, heat flow transients, and losses at the root. Because test booms are acted upon by gravity forces, this contribution must be considered in arriving at an ultimate level of static thermal bending peculiar to a given boom. (Gravity forces are considered in a later section.) To determine the manner and extent to which the above factors affect boom performance, a thin-walled Be-Cu tube having a black surface is used for calibration purposes. The very high absorptivity and emissivity of the black surface permit



Figure 1.—Thermal-mechanics test facility for deployable-boom structures.

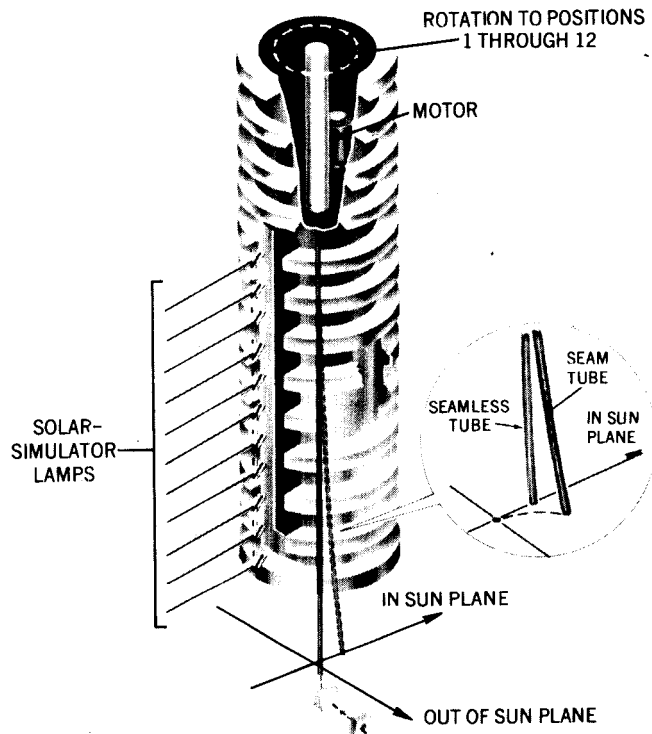


Figure 2.—Cutaway diagram of the thermal-mechanics test facility.

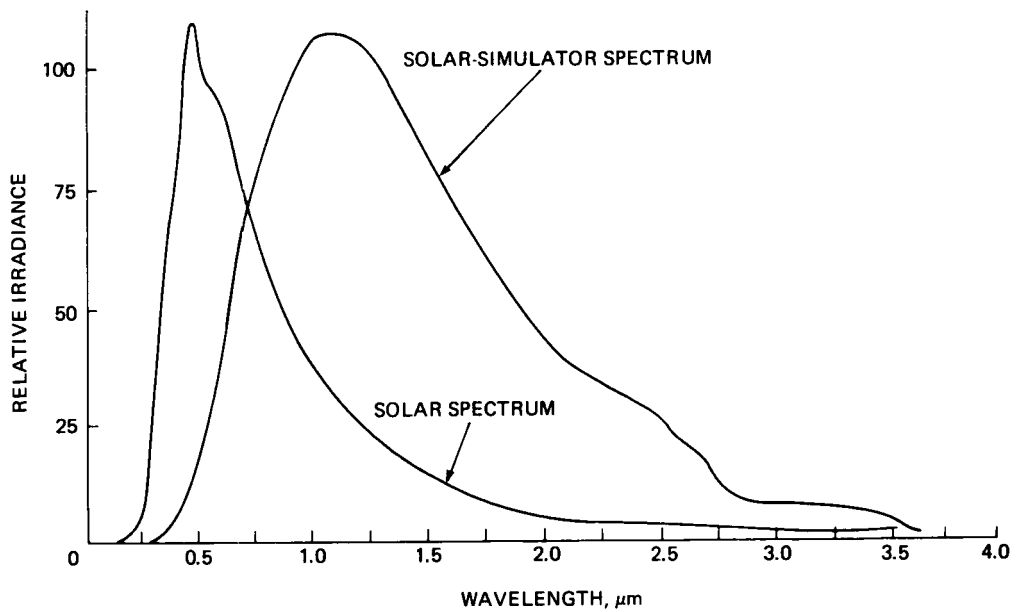


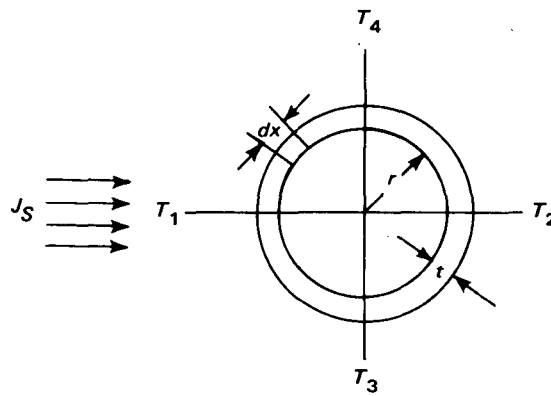
Figure 3.—Spectral distribution for sunlight and the solar simulator of the test facility.

the attainment of accurate measurement for comparison to the seamless-tube analysis, as required for calibration.

### Theory of Thermal Bending for a Thin-Walled Cylinder

The detailed theoretical analysis of the thermal bending of a thin-walled cylinder is presented in reference 5. Because of its simplicity, it is common practice to utilize this analytical treatment to scale thermal bending of booms on spacecraft. The corrections introduced for thermal transients and gravity contribution will be examined in following sections.

Briefly, for the steady state condition, heat flow around the perimeter of an elemental cross section with the Sun normal to the tube axis as shown in the sketch is given in equation (1):



$$\frac{\partial q_c}{\partial x} dx = q_r + q_i - q_s \quad \text{W} \quad (1)$$

where

$q_c$  = heat conducted around the tube, W

$q_r$  = heat radiated to space, W

$q_i$  = heat radiated across the interior of the tube, W

$q_s$  = radiant heat from the Sun absorbed at the surface of the tube, W

Substitution of the heat flow equations and use of the assumptions that  $q_i = 0$  and  $T_1/T_3 \cong 1$  (e.g., 300 K/300.5 K  $\cong 1$ ) result in

$$T_1 - T_2 = \Delta T = \frac{r^2 J_S \alpha_S}{Kt} \quad \text{K} \quad (2)$$

where

$T_1$  = maximum temperature, K

$T_2$  = minimum temperature, K

$T_3$  = mean temperature, K

$r$  = radius, m

$J_S$  = solar flux,  $W m^{-2}$

$\alpha_S$  = solar absorptivity

$K$  = thermal conductivity,  $W m^{-1} K^{-1}$

$t$  = thickness, m

Equation (2) results in a calculated maximum temperature gradient that is approximately 4 percent high (for both a 0.14-mm (5-mil)-thick black Be-Cu tube and a 0.05-mm (2-mil)-thick Be-Cu tube) because the heat radiated across the inside of the tube (ref. 5) is neglected.

When the temperature gradient across the diameter of the tube is linear or the temperature around the perimeter is a cosine function (eq. (2)), thermal bending will occur about a radius of curvature without distortion of the cross section. Under these conditions, equation (3) describes the tip deflection of a clamped-free cantilever tube exhibiting temperature-gradient uniformity along its length.

$$\delta_{0g} = \frac{e_c r L^2 J_S \alpha_S}{4Kt} \quad m \quad (3)$$

where

$\delta_{0g}$  = tip deflection at zero gravity normal to the boom axis, m

$e_c$  = coefficient of thermal expansion,  $m m^{-1} K^{-1}$

$L$  = boom length, m

### Transient Thermal Bending

It was necessary to investigate boom transient thermal behavior to ascertain the thermal time constants. These data were used to determine the time needed for the thermal gradient to establish a quasi-equilibrium condition and for development of the resulting thermal bending. The experimental results were then correlated with a transient heat flow digital analysis using the Nodal Network Thermal Balance Program.<sup>1</sup> In this approach, the cross section is divided into 24 elements running the length of the seamless tube. Heat absorption from the Sun, emission to space, internal radiation, and conduction between elements was introduced in the model. For the specific case of steady state temperature gradient and neglecting internal radiation, the digital solution agrees exactly with the analytical solution (eq. (2)). In addition, the Nodal Network Thermal Balance Program permits the solution of thermal transient problems both with and without internal radiation, assuming that the properties (absorptivity, emissivity, and thermal conductivity) remain constant.

Figure 4 graphically illustrates the transient temperatures developed between the front  $T_1$  and the back  $T_2$  of a 1.3-m (0.50-in.) nominal diameter, 0.13-mm (5-mil) thick stainless steel tube. The

---

<sup>1</sup>Developed by N. Ackerman, GSFC, June 1969.

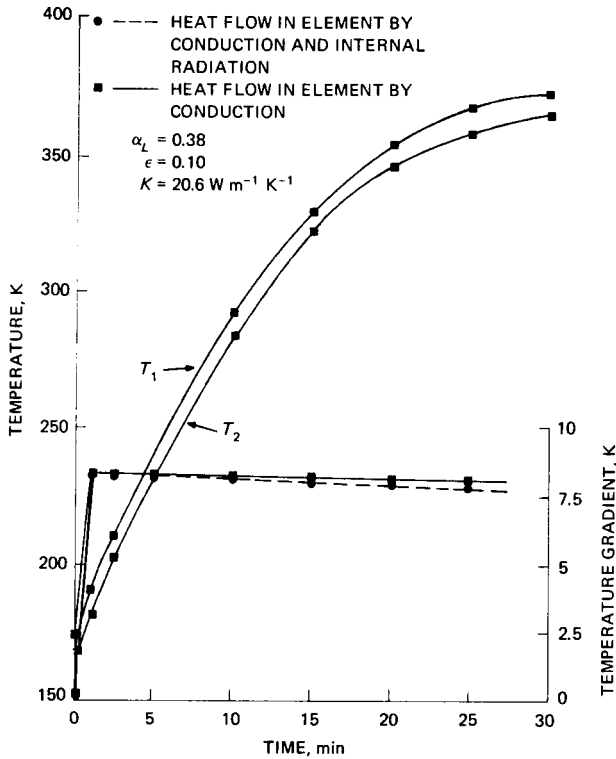


Figure 4.—Calculated transient-temperature distribution for seamless stainless-steel tube.

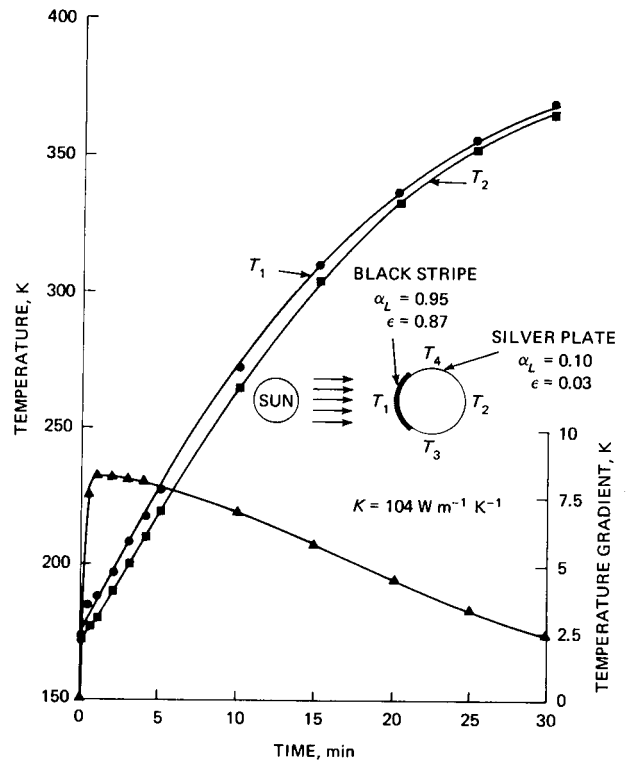


Figure 5.—Calculated transient-temperature distribution for Ag-plated Be-Cu seamless tube with black stripe.

maximum temperature gradient  $\Delta T_{\max}$  was developed during the initial transient heat flow phase at a rate controlled by thermal conductivity, as calculated with and without internal radiation. It is apparent that the temperature gradient remains essentially constant for both heat flow cases after approximately 1-min exposure, with a maximum change of less than 4 percent recorded after a period of 30 min. The observed temperature excursions can be explained as follows. At the onset, both front ( $T_1$ ) and back ( $T_2$ ) temperatures are 165 K ( $-160^\circ \text{ F}$ ) and therefore  $\Delta T_{\max} = 0$ . About 1 min after the solar simulator is turned on, a temperature gradient  $\Delta T_{\max}$  of 8.1 K ( $14.6^\circ \text{ F}$ ) is established and remains essentially constant as the boom mean temperature ( $T_3$  or  $T_4$ ) increases from 185 K ( $-125^\circ \text{ F}$ ) to more than 370 K ( $200^\circ \text{ F}$ ) for steady state equilibrium. The fact that the temperature gradient is essentially invariant a short time after heat flux exposure provides a basis for rapid measurement of temperature gradient and thermal bending at any mean boom temperature. Thus the thermal bending test for a boom of uniform emissivity simply involves turning the solar-simulator heat flux on or off for 1 min and measuring the resulting changes in boomtip position.

To illustrate the effect of nonuniform emissivity on thermal gradients, the transient temperature distribution for a 0.05-mm (2-mil) thick Ag-plated Be-Cu tube with a black vertical stripe facing the heat source was analyzed, and the results are graphically presented in figure 5. As indicated, the

temperature gradient rises to a peak ( $\Delta T_{\max} = 8.3 \text{ K (15 F}^\circ\text{)}$ ) in approximately 1 min of exposure. This is explained by the fact that at the low boom temperature, much of the heat absorbed is retained as internal energy, thus the corresponding emittance loss is negligible. However, in marked contrast to the previous case of a seamless tube of uniform emissivity, the temperature gradient drops sharply to 2.5 K (4.5 F $^\circ$ ) after 30 min of simulated irradiation. This reduction in thermal gradient occurs as the tube approaches equilibrium conditions, because approximately 70 percent of the heat absorbed is emitted by the black surface facing the heat source and thus is not conducted to the back side. Reduction of heat conduction by 70 percent leads to a comparable reduction in thermal gradient and thermal bending.

To determine experimentally the influence of the high-emissivity coating on tip deflections, a 6.5-mm (1/4-in.) wide black stripe was painted on an overlapped 1.3-cm (0.50-in.) diameter Ag-plated Be-Cu alloy boom and irradiated in the orientation shown in figure 5. In-plane and out-of-plane static bending were measured over a test period of 30 min, with the results plotted in figure 6. After achieving a tip deflection of 54 mm in the first minute, the Sun-plane bending dropped off to 20 mm, corresponding to the equilibrium temperature of 370 K (200 $^\circ$  F) for the boom. The shape of the measured thermal bending closely approximates the shape of the thermal gradient curve calculated for the Ag-plated Be-Cu alloy seamless tube with the black stripe (fig. 5). The out-of-plane bending (characteristic of the overlap boom) exhibited a similar reduction in thermal bending, as shown in the figure.

### Calculated Thermal Bending of a Perforated Seamless Tube

The temperature gradients responsible for static thermal bending are a linear function of the heat conducted from front to back. While complete elimination of such induced temperature gradients is not possible, considerable

reduction in  $\Delta T_{\max}$  can be achieved within acceptable levels by incorporating highly reflective external coatings, high-absorptance interior coatings, and perforations to homogenize the solar heat flux impinging on both front and back surfaces. The optimum optical properties of both internal and external surfaces and an appropriate percentage of perforations can be found from the following equation (ref. 5):

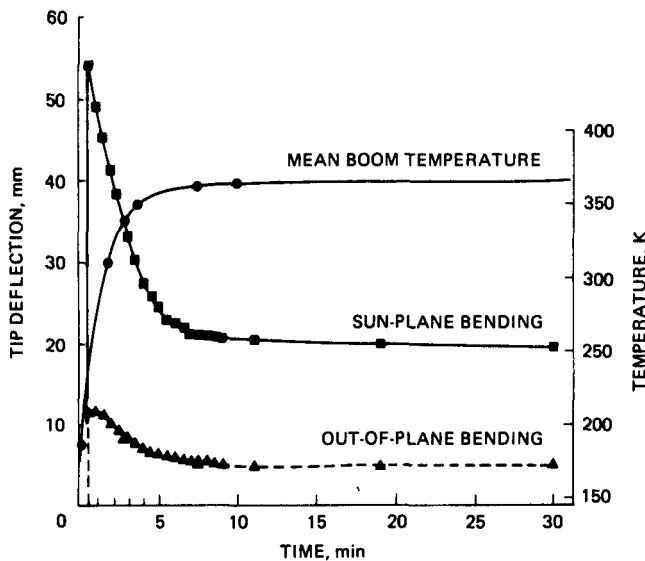


Figure 6.—Observed thermal bending and transient mean temperature for Ag-plated, overlapped Be-Cu tube with black stripe.

$$\delta_{0g} = \frac{e_c r L^2 J_S (1 - P)}{4Kt}$$

$$\times \left[ \alpha_S - \frac{P\beta_S}{1 + (1 - P)(1 - \beta_S)} \right] \quad (4)$$

where

$P$  = fraction of surface area removed

$\beta_S$  = absorptivity of inner surface

The temperature gradients in a perforated seamless tube or similar boom configuration can thus be minimized, resulting in essentially zero in-plane bending.

### Calibration of Measurements: Bending of a Black Seamless Tube

For the reasons given earlier, a black seamless tube was employed to calibrate thermal bending measurements. In addition, the effects of vacuum and temperature on the surface properties of this tube are considered negligible. Table A-1 presents the properties and results obtained for the black Be-Cu test tube. The mechanical, thermal, and electrical properties of Be-Cu alloy 25 are related directly to its thermal-mechanical condition. Thus accurate thermal conductivity for a given thermal-mechanical condition can be obtained using measured electrical conductivity data and the Wiedemann-Franz law (ref. 6). The effect of temperature on thermal conductivity is shown in figure 7 for two Be-Cu alloys.

The measurement of solar-simulator heat flux  $J_L$  is checked by determining the mean, steady state temperature of the black tube and employing equation (5):

$$J_L = \frac{\sigma \pi \epsilon}{\alpha_L} \left( \frac{T_3}{100} \right)^4 \quad \text{mW cm}^{-2} \quad (5)$$

$\sigma$  = Stefan-Boltzmann constant  
 $= 5.67 \times 10^{-8} \text{ W m}^{-2} \text{ K}^{-4}$

$T_3$  = mean temperature, K

$\epsilon$  = emissivity

$\alpha_L$  = solar-simulator absorptivity

For a measured mean temperature of 302 K, the calculated heat flux is  $137 \text{ mW cm}^{-2}$ , which is in very good agreement with the value of  $138 \text{ mW cm}^{-2}$  measured with an Eppley radiometer.

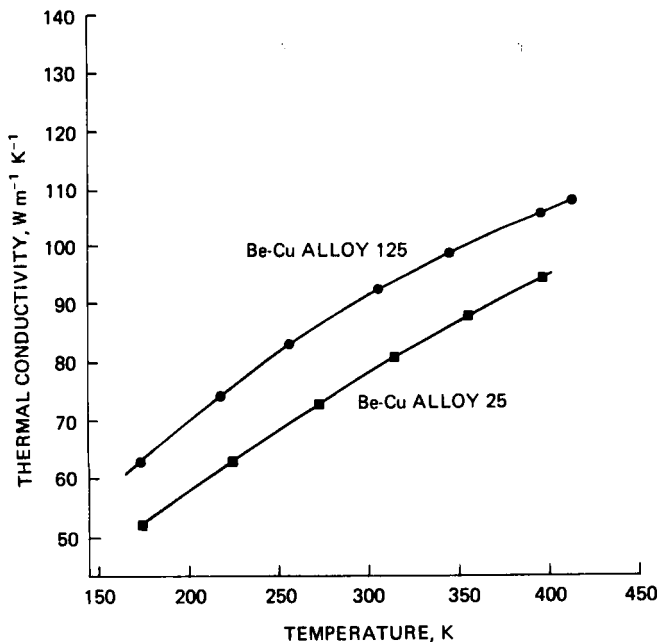


Figure 7.—Temperature effect on thermal conductivity of Be-Cu alloys.

Linear deflection theory used in the derivation of equations (2) and (3) assumes that the temperature distribution around the perimeter follows a cosine function. This was confirmed experimentally and the results are presented in figure 8. The test procedure involved positioning the black Be-Cu tube in the vacuum chamber, which was operated at  $10^{-5} \text{ N m}^{-2}$  ( $10^{-7}$  torr). Thermocouples had been welded to the front and back of the tube with a

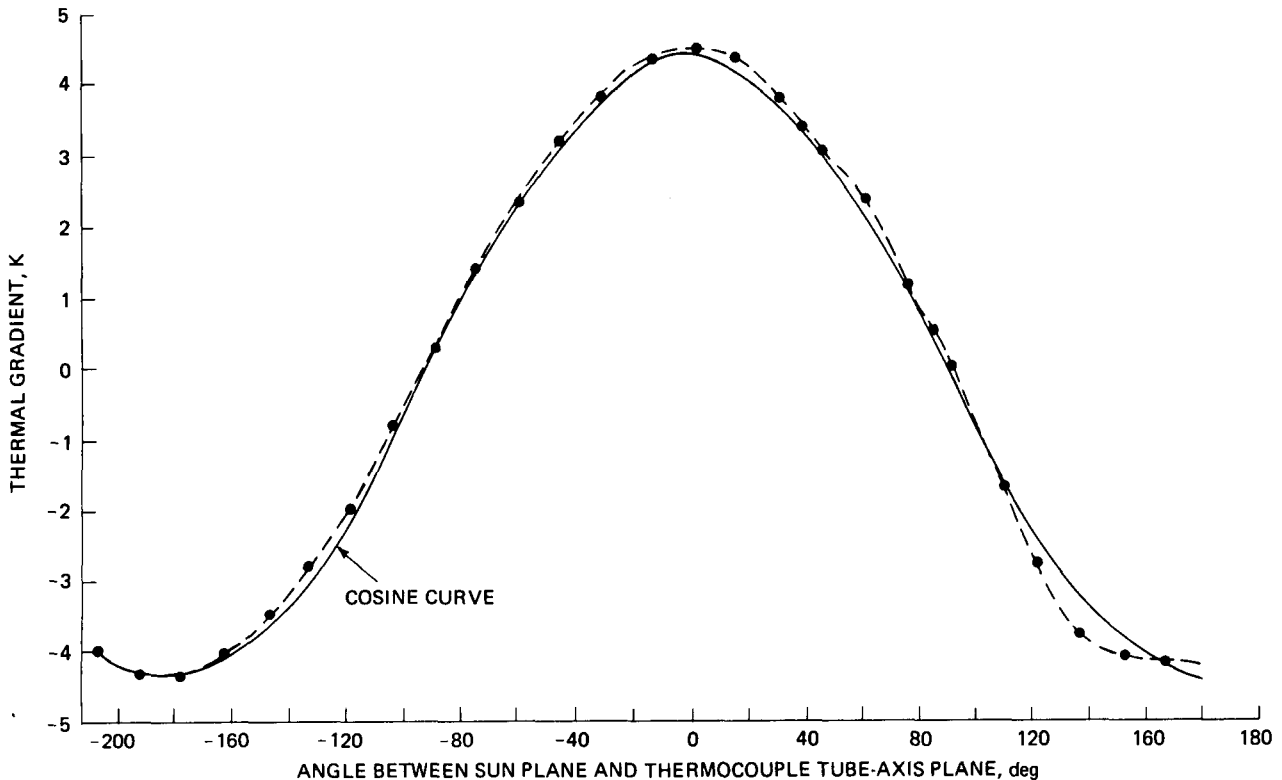


Figure 8.—Temperature gradient versus Sun angle for black Be-Cu seamless tube.

potentiometer connected in series with each. Their outputs were monitored on a recorder. After heating the boom from approximately 140 K ( $-200^{\circ}$  F) to a mean temperature of 240 K ( $-25^{\circ}$  F), the solar simulator was turned off and the potentiometers were adjusted to give the same emf. The simulator was then switched on and after 1 min the difference in thermocouple response (emf) was measured. This process was repeated for 26 Sun angles giving the results shown in figure 8 with a superimposed cosine curve.

The relatively good agreement between a cosine function and the measured temperature distribution around the perimeter shows that this assumption for equations (2) and (3) is valid with a seamless tube. The absolute value for temperature gradient,  $\Delta T_{\max} = 4.3$  K ( $7.7$  F $^{\circ}$ ), is not accurate because of local variations of heat flux along the length of the solar-simulator field and errors caused by stray potentials along the 4.6-m (15-ft) thermocouple wires.

The variation of temperature gradient is solely responsible for thermal bending response. The static thermal bending over a period of 2 hr, plotted in figure 9, indicates that maximum bending is achieved in approximately 1 min. This is essentially the same time that was calculated to achieve maximum temperature gradient as discussed earlier and shown in figure 4. During this test period, the average boom temperature increased from 140 to 370 K ( $-200^{\circ}$  to  $200^{\circ}$  F), while thermal bending

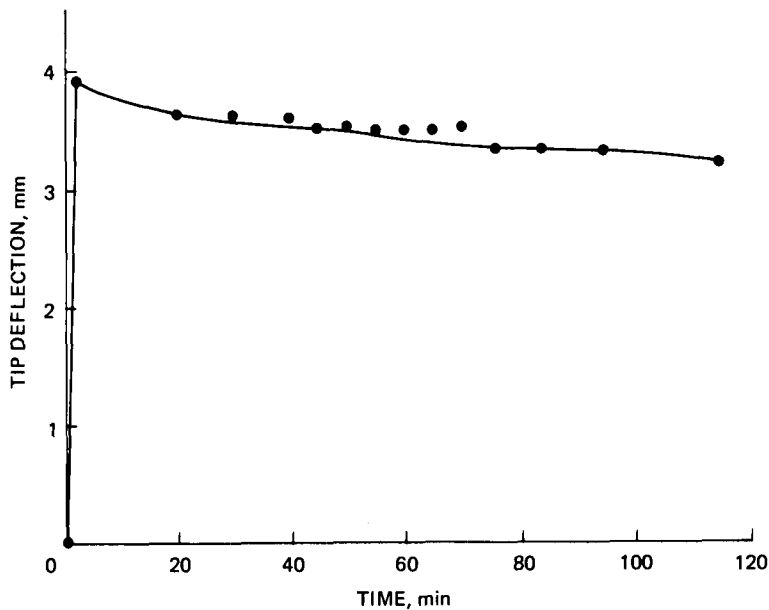


Figure 9.—Sun-plane thermal bending of Be-Cu seamless tube.

decreased from 4 to 3.2 mm. This reduction in thermal bending is easily explained by noting that the thermal conductivity also increased from  $50 \text{ W m}^{-1} \text{ K}^{-1}$  (29 to 46 Btu/hr °F ft) at the higher temperature.

Fabrication practices usually preclude the attainment of perfectly straight booms, as shown in table A-1. In view of this, much work was performed to insure that the experimental procedure employed was unaffected by the quality of the boom even in 30-m (10-ft) lengths. The following illustrates the method of conducting thermal bending measurement, using a 0.14-mm (5-mil) Be-Cu seamless tube with 34.6-mm (1.36-in.) tip distortion due to fabrication. Measurements were obtained at 12 orientations in increments of  $30^\circ$  rotation. Tip position angle was accurately measured to  $\frac{1}{4}''$  using a theodolite and mirror arrangement with the simulator turned off. Then the procedure was repeated 30 s after the solar simulator was switched on and the angular difference was computed. The differences in both Sun-plane and out-of-plane angular components were converted to millimeters, using the calibration constant of  $59'' \text{ mm}^{-1}$ . The results are plotted in figure 10 and clearly demonstrate a classical example of Sun-plane bending, reaching a magnitude of 4.24 mm with no out-of-plane bending or thermal static twist. The relative accuracy of boomtip deflection measurements from Sun position to Sun position is about 0.1 mm. The temperature gradient of a black Be-Cu seamless tube was calculated from the optical properties and compared with the same temperature gradient calculated from the measured tip deflection to determine the absolute accuracy of the thermal bending measurements.

The thermal bending observed at 297 K (75° F) for the black tube was 2.570 cm (1.012 in.). Applying a gravity correction (given in eq. (7)), the value increases slightly to 2.868 cm (1.129 in.). Calculating the corresponding maximum temperature gradient from the measured thermal bending,

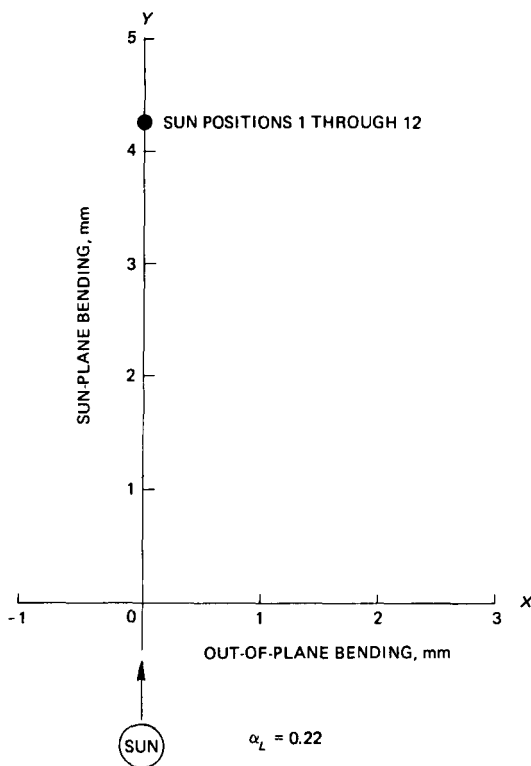


Figure 10.—Transient thermal bending of seamless Be-Cu tube at 12 Sun-angle orientations.

with thermal distortion of the vacuum chamber itself, thermal gradient errors around the base of the boom due to the large mandrel, and thermal distortion of the supporting mandrel. To measure the thermal bending of the chamber and the mandrel, a 3.0-m (10-ft) solid invar rod was clamped to a mandrel of the same material, thus providing a calibration element that exhibited essentially zero thermal expansion. After 10 min of thermal soaking, sufficient to achieve a temperature gradient of 10 K (18 F°) across the mandrel, no significant bending was observed. However, after an additional hour of solar simulation exposure, the rod tip exhibited a displacement of 0.28 mm toward the solar simulator, which is wholly attributed to differential heating and bending of the chamber. Because most measurements are made in approximately 1 min, this factor can be dismissed as a possible source of bending error.

The support mandrel has a very large thermal mass compared with the thin-walled tube attached to it. Thus significant end effects (thermal losses) could introduce variations in thermal gradients in the boom. In addition, the fact that the support assembly passes through the top of the chamber subjects this section to a sink temperature of approximately 295 K (70° F), further accentuating this problem. A 0.13-mm (5-mil) stainless steel tube was instrumented with thermocouples positioned 5 and 15 cm (2 and 6 in.) below the support mandrel. Under steady state conditions, the mandrel

using equation (6), yields 4.8 K (8.6 F°):

$$\Delta T_{\max} = \frac{4r\delta_{0g}}{e_c L^2} \quad \text{K} \quad (6)$$

where factors are as previously defined. It must be noted that  $\Delta T_{\max}$  calculated from thermal bending data actually represents a mean of the gradients generated along the entire length of boom. Thus, any local variations in the light field or thermocouple response are essentially averaged out. The thermal gradient for the black Be-Cu tube was also calculated from its optical constants, using equation (2). At 297 K (75° F) the calculated  $\Delta T_{\max}$  was 5.5 K (9.9 F°), using the solar-simulator absorptivity of 0.95, yielding a value 13 percent larger than the 4.8 K (8.6 F°) determined from the thermal bending measurement.

However, equation (2) predicted a thermal gradient 4 percent greater than expected because internal radiation heat transfer was neglected. This correction reduces the discrepancy to 9 percent. The measured thermal bending is thus demonstrated to be accurate within 9 percent of the value calculated from seamless-tube theory. Part of the 9-percent error is associated

temperature registered 289 K (60° F) while the boom thermocouple 5 cm (2 in.) below the mandrel reached 365 K (197° F), which represented the equilibrium temperature for that particular boom structure. The corresponding temperature gradient measured across the tube diameter 5 cm (2 in.) below the support mandrel remained essentially constant at 9.5 K (17 F°). This characteristic is repeatable and indicates that upon reaching equilibrium conditions, the segment in the vicinity of the root is thermally unaffected by the support assembly, and therefore errors stemming from end effects can be ignored.

### Thermal Bending of a Be-Cu Seamless Tube

Unlike the black Be-Cu calibration specimen, the measured bending of a Be-Cu seamless tube (shown in table A-2) did not agree with the thermal bending calculated from optical constants and seamless-tube theory. The measured solar or solar-simulator absorptivity (ref. 7) varies by less than 1 percent for silver and stainless steel from one measurement apparatus to the next. Examples of the solar and solar-simulator absorptivity measurements are presented in tables A-3 and A-4 for a sample of the Be-Cu seamless tube. Measurement errors could not account for the observed discrepancy. Comparison of observed values and the calculated values for the black seamless tube showed the errors to be less than 9 percent, therefore the discrepancy is not caused by the theory for seamless tubes. However, the measurements of absorptivity along the length of the boom were found to vary by a factor of approximately 2. In addition, the effects of vacuum and surface temperature are unknown. Therefore, the large differences between observed and calculated thermal bending for the Be-Cu seamless tube are attributed to the fact that the absorptivity measured on a small sample under ambient conditions does not represent the average boom absorptivity in vacuum at various temperatures.

### Gravity Loading of a Thermally Bent Tube

As indicated earlier, the vertically clamped boom is restrained by gravity forces from assuming the true thermal bending profile due solely to solar simulation. The effect of gravity on a 3.0-m (10-ft) boom was investigated analytically and is described by the following equation:

$$\delta_{1g} = \delta_{0g} \left( 1 - \frac{7WL^3}{60EI} \right) \quad (7)$$

where

$\delta_{1g}$  = tip deflection at 1g load from thermal bending, m

$W$  = weight per linear unit, N m<sup>-1</sup>

$EI$  = tube stiffness, N m<sup>2</sup>

Equation (7) is derived for a 1g load along the axis of the clamped-free parabolic tube in a stress-free state. For the 3.0-m (10-ft) booms employed in this investigation, a reduction in magnitude of thermal bending of less than 12 percent caused by gravity effects is calculated.

## EXPERIMENTAL RESULTS FOR VARIOUS BOOM TYPES

Phenomenologically, boom bending can be explained in terms of temperature gradients and the consequent development of differential thermal expansions occurring between the surface exposed directly to solar irradiation and the side opposite. For example, a seamless tube presents an ideal condition of complete thermal symmetry; i.e., the heat conduction path is circumferentially identical about the Sun plane. Thus, this situation gives rise to the classical case of Sun-plane bending as shown earlier in figure 10. By introducing a geometrical discontinuity such as an interlocking seam, the temperature distribution becomes more complex and heterogeneous. In this event, the thermal conductive path is not symmetric about the circumference, resulting in out-of-plane bending possibly coupled with a thermal static-twist component. The extent of the thermal dissymmetry is chiefly dependent on the type of interlocking construction and the thermal conductivity characteristic developed across the seam interface. The orientation of the incident flux impinging on the boom element relative to the coordinate system employed is shown in figure 11. Similarly, figure 12 defines four of the basic Sun positions used in determining tip distortion of the element. (Orientation angle is measured in either 12 or 36 steps.)

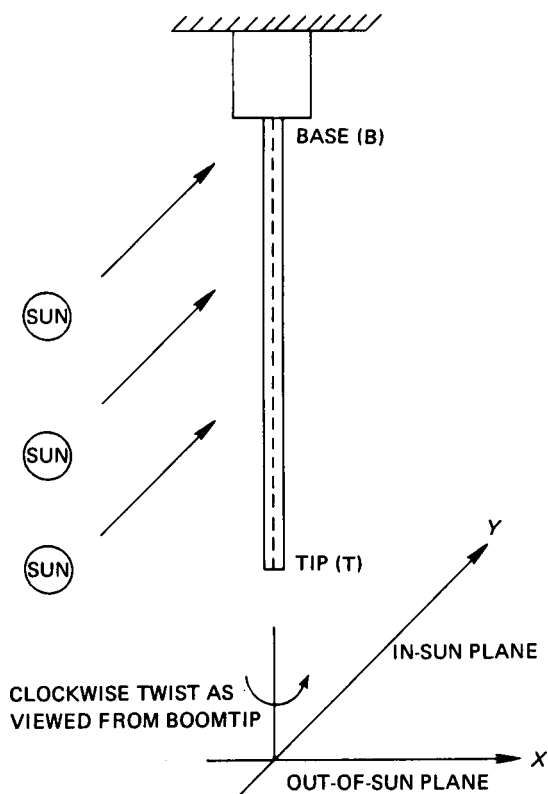


Figure 11.—Solar-simulator, boom-orientation coordinate system.

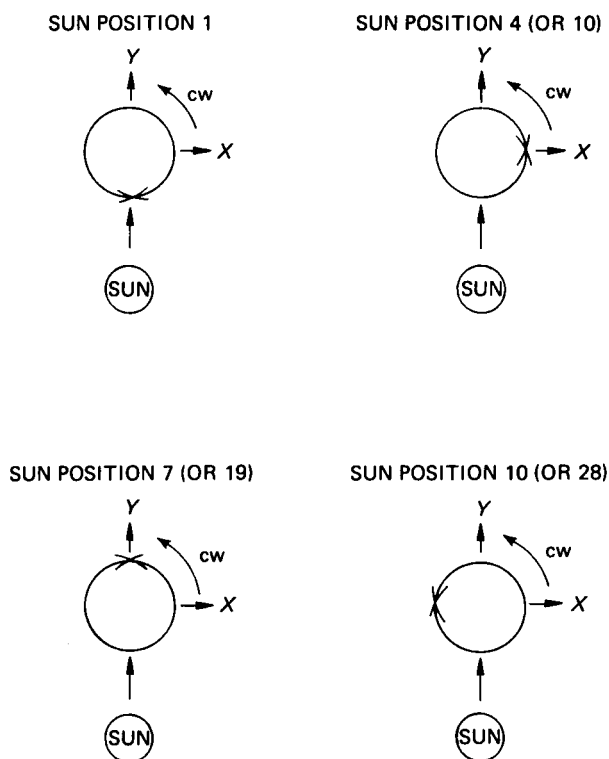


Figure 12.—Sun positions designated at test-boom tip.

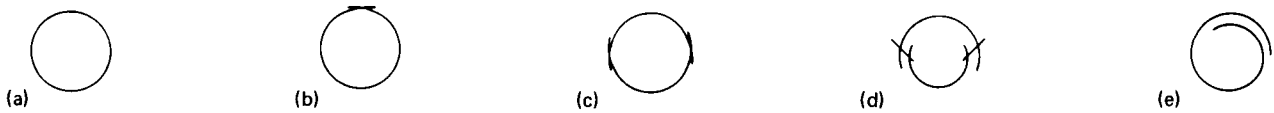


Figure 13.—Cross sections of boom design concepts. (a) Seamless tube. (b) Interlocked. (c) Hinge locked. (d) Interlocked BI-STEM. (e) Overlapped.

The boom design configurations investigated are presented in figure 13. A simple seamless tube was employed for both comparative and calibration purposes. The various test elements can be reduced to three basic seam-joining concepts:

- (1) The interlocking design involves self-meshing of serrated edges during deployment. This action arises from an induced memory developed in the metal strip, which causes it to form into a circular configuration as it rolls off a drum.
- (2) The Hingelocked concept requires that the two halves be mechanically zippered because the strip has not been metallurgically preconditioned.
- (3) The interlocked BI-STEM essentially consists of a boom nesting within a boom in which tabs of one element forcibly engage slots in the mating element.

In addition, a rigidized wire-screen boom with large open area was tested. The following sections discuss the thermal bending performance of the various test elements; more details are given in the tables in appendix A.

#### Be-Cu Interlocked (Westinghouse)

The interlocked seam is essentially straight along its 3.02-m (10-ft) length and its bare Be-Cu surface exhibits a solar-simulator absorptivity  $\alpha_L$  of 0.19. Using the coordinate system of figures 11 and 12, thermal static bending for 12 Sun positions in increments of  $30^\circ$  clockwise (cw) rotation is shown in figure 14(a). To demonstrate the effect of fixing the boom element while rotating the source about the element, the data were replotted in polar form as shown in figure 14(b). It is apparent from these data that the Sun-plane bending vector is about six times longer than the out-of-plane bending. The relatively small out-of-plane bending is attributed to the low seam interference to heat conduction. For this element no significant thermal static twist was observed within the measurement limits of about  $\pm 10^\circ$  for all orientations. As noted in figure 14(a), the out-of-plane bending profile is essentially symmetric, with the maximum out-of-plane components occurring at Sun positions 4 and 10 in the direction of the seam. When reduction in heat conduction at the seam was sufficient to lower the seam temperature relative to the solid section on the opposite side of the boom, the observed out-of-plane bending moved in the seam direction.

#### Ag-Plated Be-Cu Interlocked (Fairchild-Hiller)

This boom concept flew as the root section of the booms on the RAE A satellite (ref. 8). Its solar-simulator absorptivity was reduced to 0.04 by silver plating. The thermal bending profile for this element is presented in figure 15. The advantage of the silver plating over an unplated Be-Cu surface is readily evident in terms of the magnitude of Sun-plane bending that occurred. In this case the

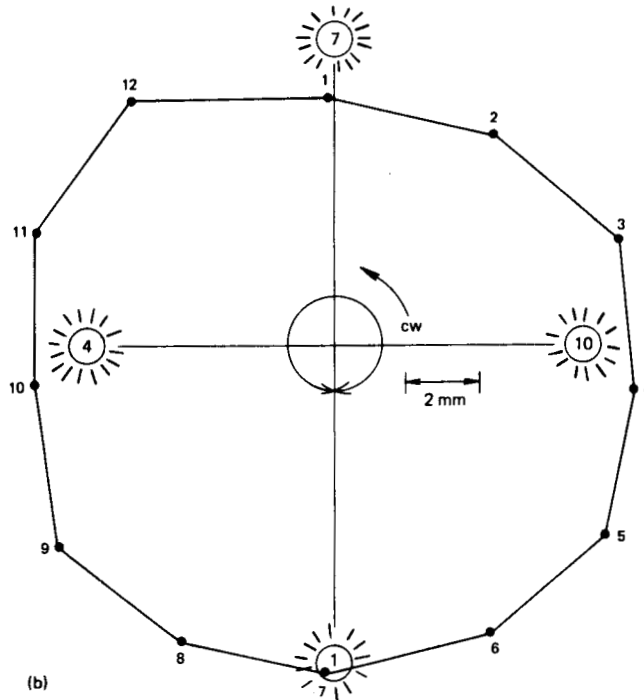
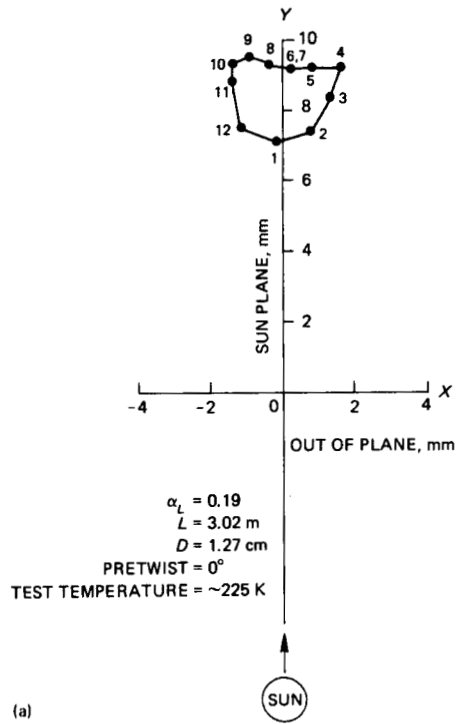


Figure 14.—Be-Cu interlocked Westinghouse boom with 0 percent perforation, test boom 1. (a) Observed coordinates. (b) Sun-rotation coordinates.

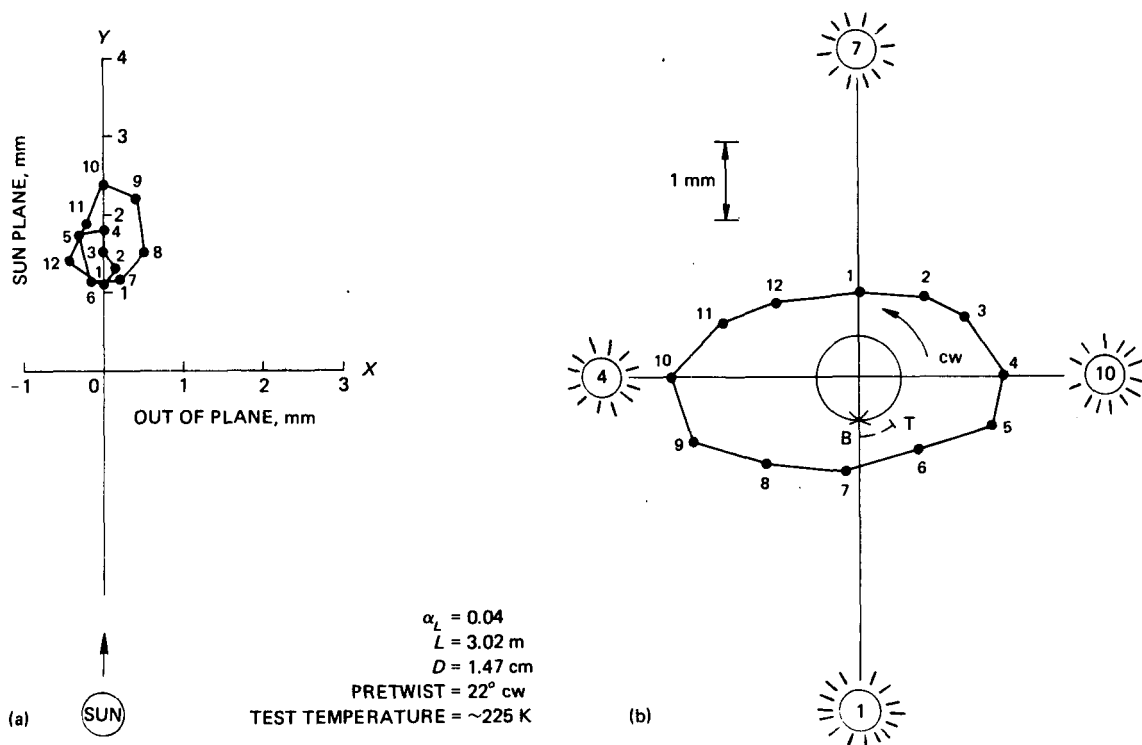


Figure 15.—Ag-plated Be-Cu interlocked Fairchild-Hiller boom with 0 percent perforation, test boom 2.  
(a) Observed coordinates. (b) Sun-rotation coordinates.

ratio of Sun-plane to out-of-plane bending was approximately 4. Sun positions 10 and 4 developed the largest in-plane bending vectors. This was not unexpected, because the concept is essentially the same as the unplated boom; i.e., both employ zippered seams, the only basic difference being in the optical properties exhibited by each. The marked increase in boom deflection observed for Sun positions 10 and 4 over positions 1 and 7 is largely attributed to the significant rise in temperature gradients at the former Sun orientation by almost a factor of 2 above the latter orientation, because the seam reduced the heat conduction from front to back of the boom by a factor of 2.

### Ag-Plated Be-Cu Hingelock (Fairchild-Hiller)

The thermal static bending characteristics of this Hingelock concept are presented in figure 16. The most striking feature of the plot in figure 16(a) is that it approaches the classical case of pure Sun-plane bending although its magnitude is comparable to the previous boom configuration. The minimum Sun-plane bending would be expected for Sun positions 1 and 7, where the incident flux is absorbed on the front side and conducted to the back of both half sections of the boom without the necessity of bridging a seam, thus resulting in a minimal temperature gradient  $\Delta T_{\text{max}}$ . This prediction was demonstrated experimentally as shown in figure 16(b). In contrast, for positions 4 and 10 the heat path must cut across two seams that thermally retard conduction and result in maximizing the temperature gradient across the boom diameter. The substantial increase in corresponding thermal static bending is confirmed by the results of figure 16(b).

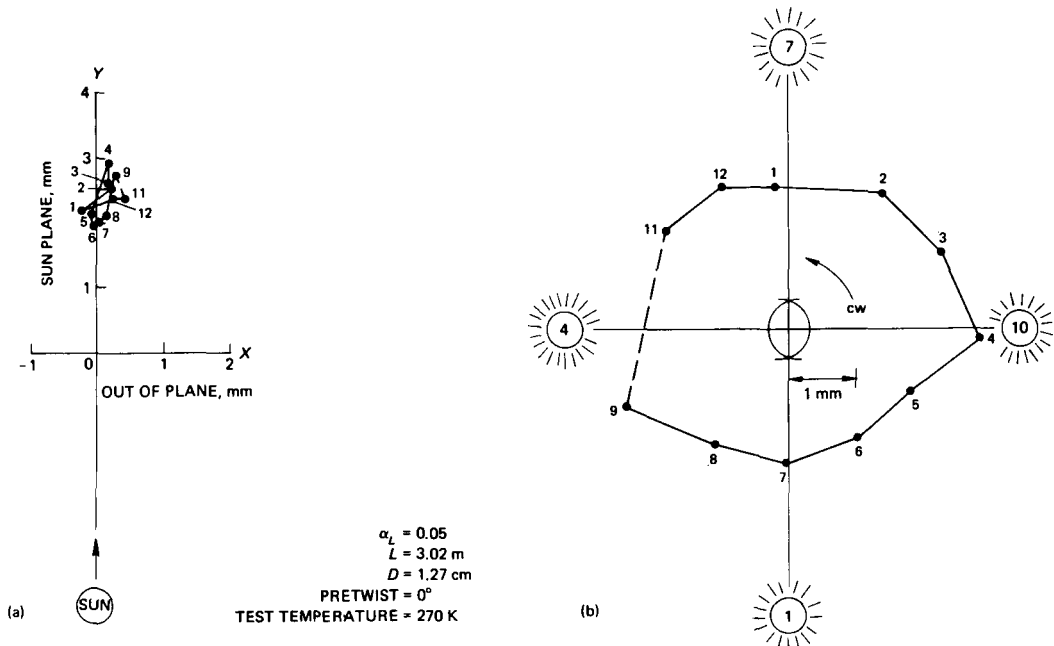


Figure 16.—Ag-plated Be-Cu Fairchild-Hiller Hingelock boom with 0 percent perforation, test boom 3. (a) Observed coordinates. (b) Sun-rotation coordinates.

### Be-Cu Interlocked (Fairchild-Hiller)

Originally, the Nimbus D satellite was to fly an experimental boom having an overlapped seam configuration. Subsequently, the desirability for increased torsional rigidity resulted in modifying this concept to accommodate a digitated seam design developed by the General Electric Co. The resulting 2.30-cm (0.91-in.) diameter boom exhibited a 15° counterclockwise (ccw) pretwist along its 3.02-m (10-ft) length.

The thermal bending profiles (fig. 17) corresponding to test temperatures of 230 and 365 K (−50° and 200° F) show reasonable similarity, although the magnitude of static bending is greater at the lower temperature. This is explained by the increase in thermal conductivity at the higher temperature and the consequent decrease in temperature gradient. While the thermal static bending pattern is similar to those obtained on previous boom configurations reflecting a single interlocking seam, the out-of-plane bending showed a definite bias at both test temperatures. No thermal static twist was observed.

### Ag-Plated Be-Cu Interlocked BI-STEM (SPAR), ½ in.

The seam of this boom design is deliberately spiraled about the axis of the element; consequently it was not surprising to measure a fabricated pretwist of 170° ccw in a length of 3.02 m (10 ft). The thermal bending response of this 1.30-cm (0.51-in.) boom is shown in figure 18. The out-of-plane bending is about a third of the Sun-plane bending observed. The lack of symmetry at seam positions 1 and 7 and 4 and 10 can be attributed in large part to the excessive pretwist in the boom, which complicates the heat transfer pattern around the perimeter for any orientation. Thus, the continuous

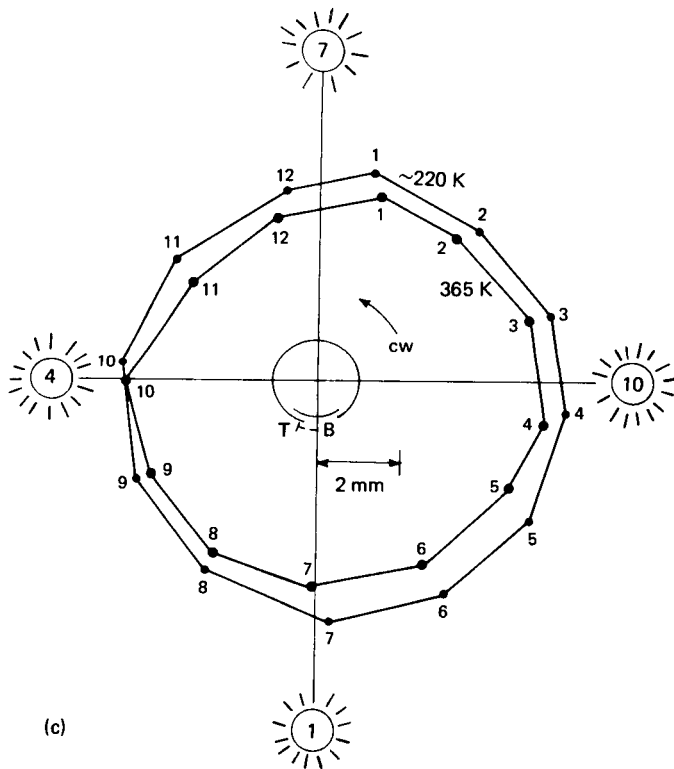
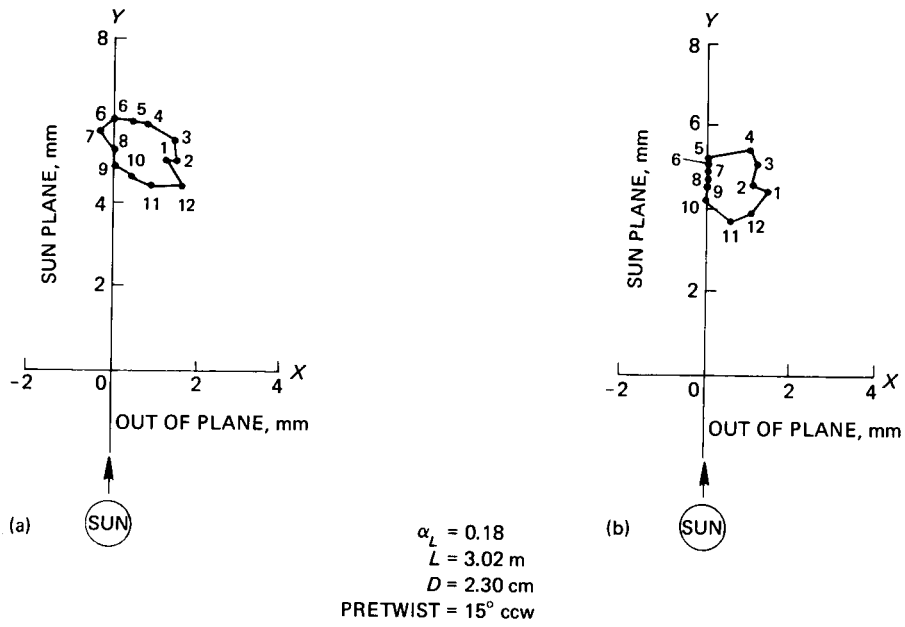


Figure 17.—Be-Cu interlocked Nimbus D boom with 0 percent perforation, test boom 4. (a) Observed coordinates, 230 K. (b) Observed coordinates, 365 K. (c) Sun-rotation coordinates.

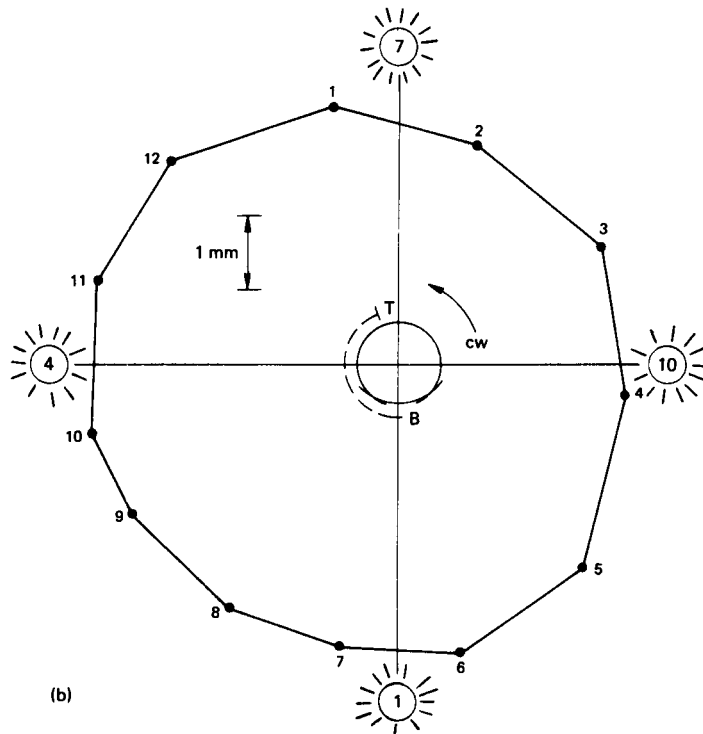
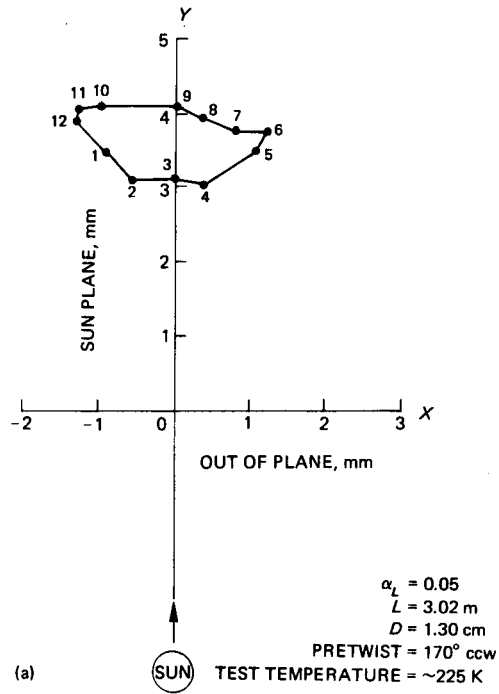


Figure 18.—Ag-plated Be-Cu interlocked SPAR BI-STEM boom with 0 percent perforation, test boom 5. (a) Observed coordinates. (b) Sun-rotation coordinates.

variation of Sun angle with respect to the seam produced a thermal bending curve (fig. 18(b)) that could not easily be explained by heat flow around the boom element. If there had been a complete 360° spiral, it is conceivable that the thermal static profile would have approached seamless-tubelike behavior.

#### **Ag-Plated Be-Cu Interlocked BI-STEM (SPAR), ¼ in.**

This boom is essentially identical to the previous configuration except that it is only 0.71 cm (0.28 in.) in diameter and has a pretwist of 315° ccw in 3.02 m (10 ft). The thermal static bending profiles at two different temperatures were similar, as shown in figure 19. As in the case of the Nimbus boom (fig. 17), static bending was less at the higher temperature because of the improvement in thermal conductivity of Be-Cu at 315 K (110° F) relative to 195 K (-110° F).

#### **Be-Cu Perforated, Interlocked (Westinghouse)**

The thermal static bending profile for this unplated boom element (refs. 6 and 8) is presented in figure 20. The pattern indicated is as expected for a single-zippered boom. That is, maxima for both Sun-plane bending and out-of-plane bending occur at orientations 4 and 10. In this configuration, the out-of-plane bending invariably occurs in the direction of the seam. Comparison of these results with the previously discussed configuration by the same manufacturer (fig. 14) suggests that the introduction of perforations alone plays only a minor role in reducing static thermal bending.

#### **Al-Black-Coated, Perforated, Interlocked (Westinghouse)**

In an attempt to reduce thermal bending of this concept, the exterior surface was plated with aluminum, while the interior surface received a black oxide treatment such that the ratio of internal to external  $\alpha_L$  was approximately 6. This factor, combined with the helical hole pattern and the introduction of a deliberate spiral during the forming process, was responsible for the thermal bending characteristic displayed by this configuration, shown in figure 21. The sharp reduction in Sun-plane bending compared to the two similar, previously mentioned Westinghouse booms is self-evident, but the peculiarity of the out-of-plane bending pattern was wholly unexpected. The explanation could well lie in the fact that the prescribed spiral of the seam did not homogenize the impinging heat flux about the boom axis as predicted by equation (4). Certainly, the fact that the interior seam is black and does not exhibit the same degree of perforation as the rest of the element surface could well lead to the behavior exhibited by the black-striped element and presented earlier in figures 5 and 6.

#### **Al-Black-Coated, Perforated, Interlocked, Low Pretwist (Westinghouse)**

To further explore the unusual thermal behavior observed on the previous boom, another element was selected with a measured pretwist of only 15° cw and all other parameters essentially the same. The graphical results of a 36-position survey of thermal static bending are shown in figure 22. Maximum Sun-plane bending occurred at position 1, where the effect of seam shadowing was most pronounced, resulting in a large temperature gradient and consequent bending. In Sun positions 10 and 28, where the plane of the seam is perpendicular to the incident source, the out-of-plane bending vector dominates in the direction of the cold seam. In these two orientations no shadowing of the back side by the seam occurs, so that the Sun-plane bending component is considerably reduced in

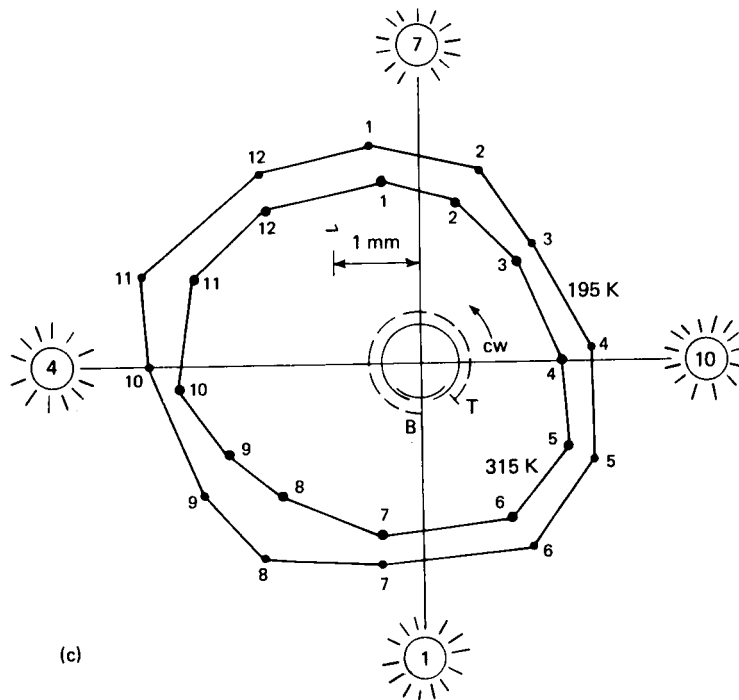
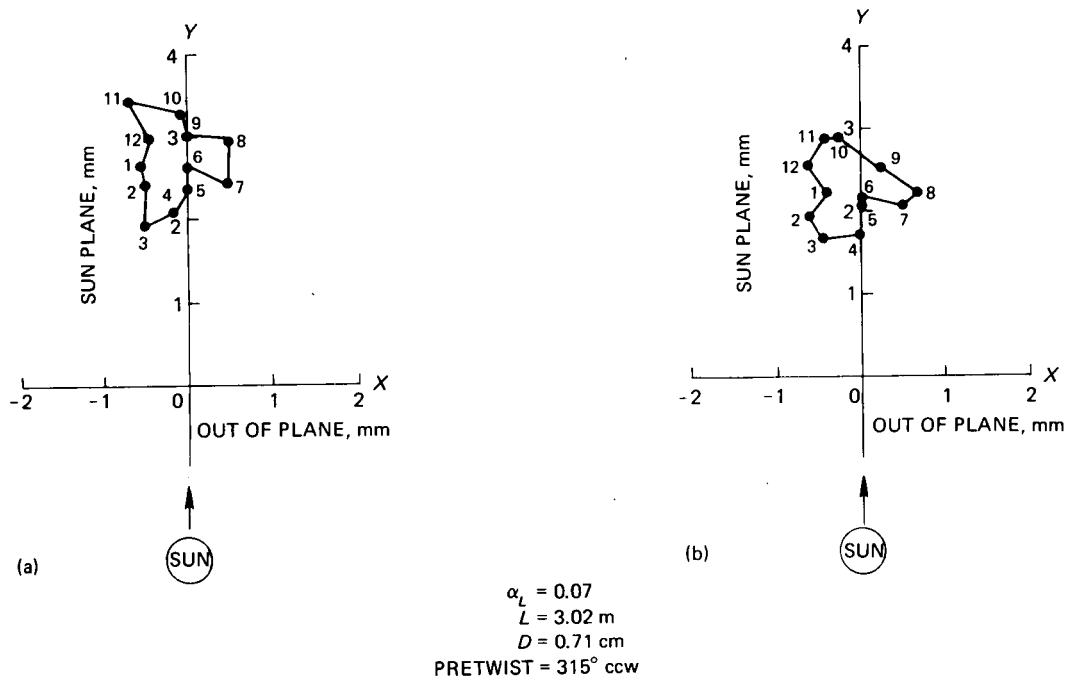


Figure 19.—Ag-plated Be-Cu Interlocked SPAR BI-STEM boom with 0 percent perforation, test boom 6. (a) Observed coordinates, 195 K. (b) Observed coordinates, 315 K. (c) Sun-rotation coordinates.

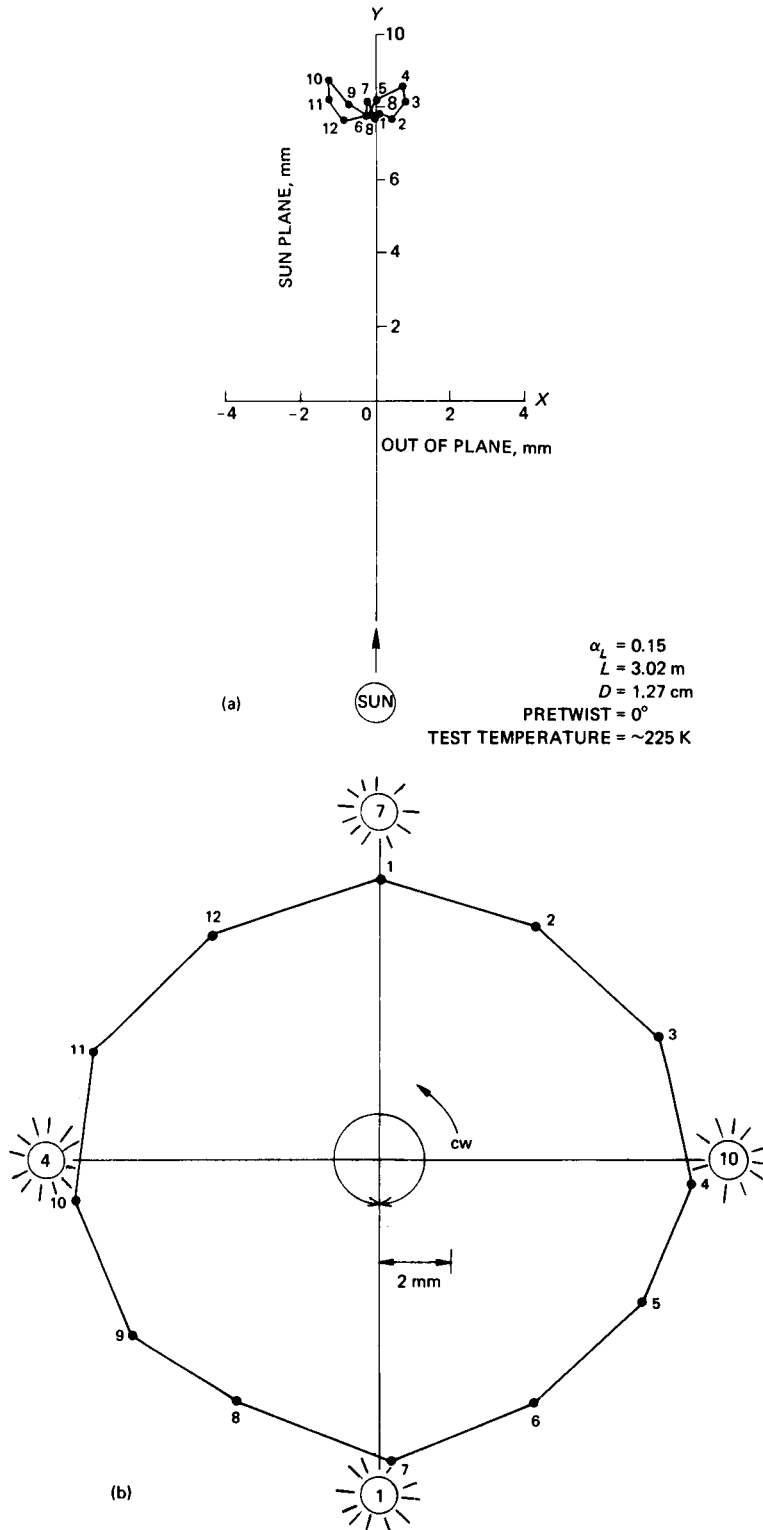


Figure 20.—Be-Cu interlocked Westinghouse boom with 15 percent perforation, test boom 7. (a) Observed coordinates. (b) Sun-rotation coordinates.

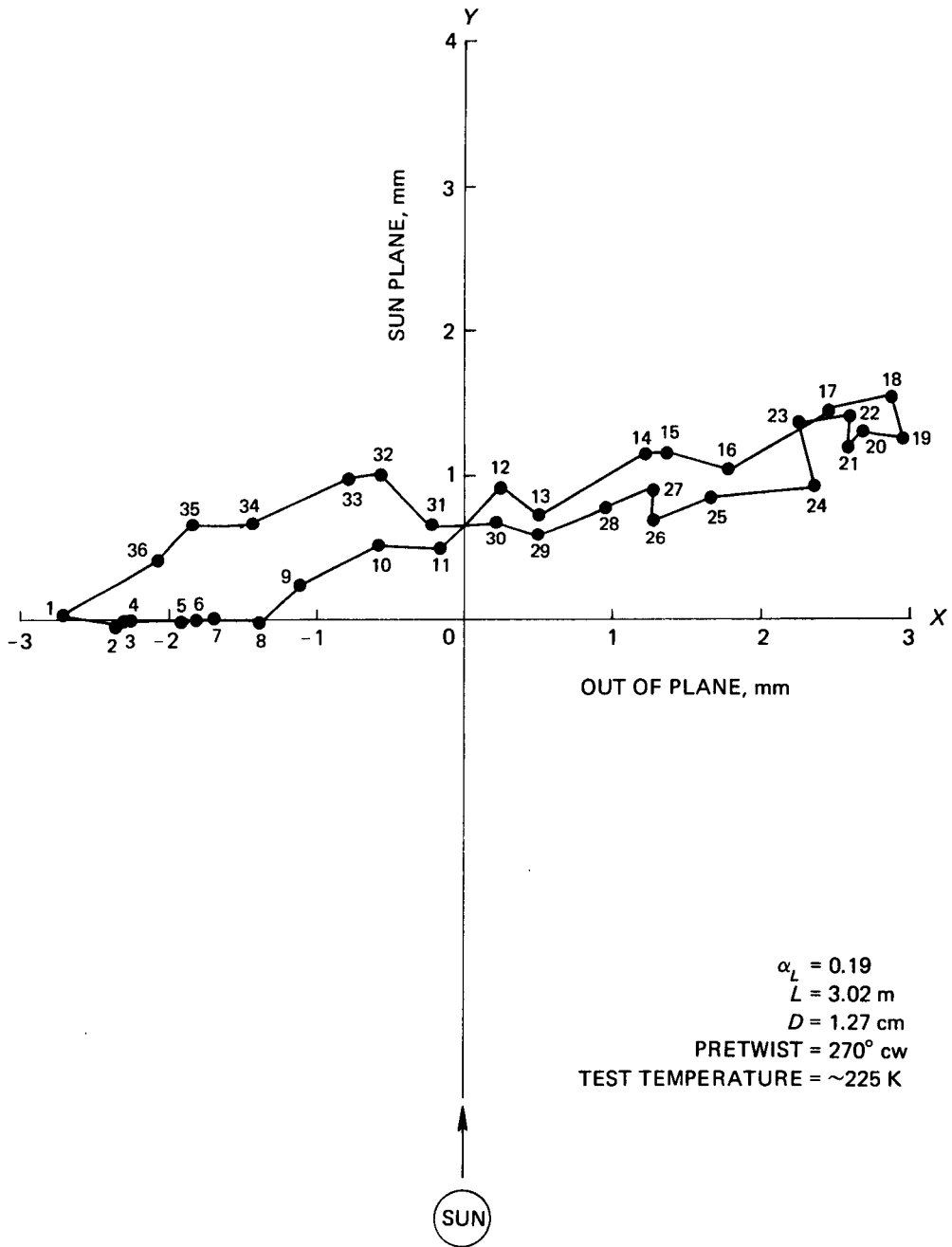


Figure 21.—Al-black coated, interlocked Westinghouse boom with 15 percent perforation and large pretwist, test boom 8. Observed coordinates.

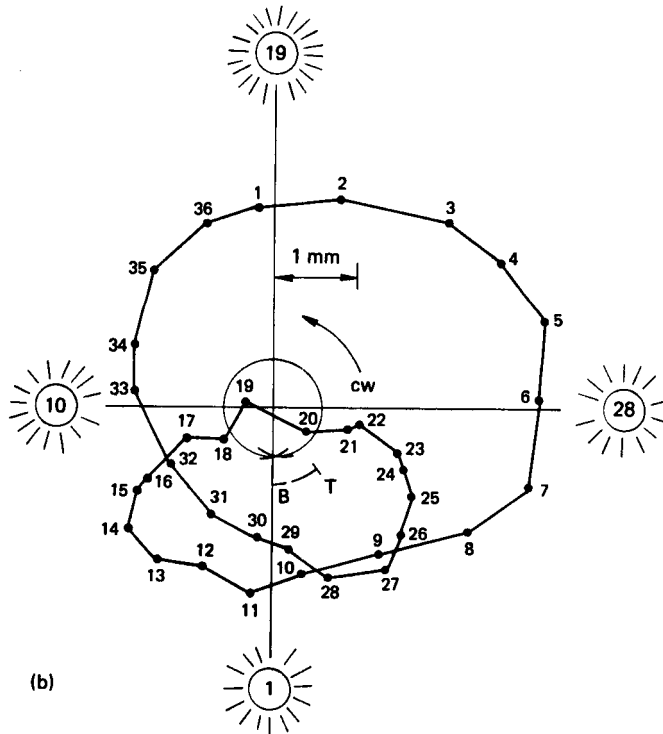
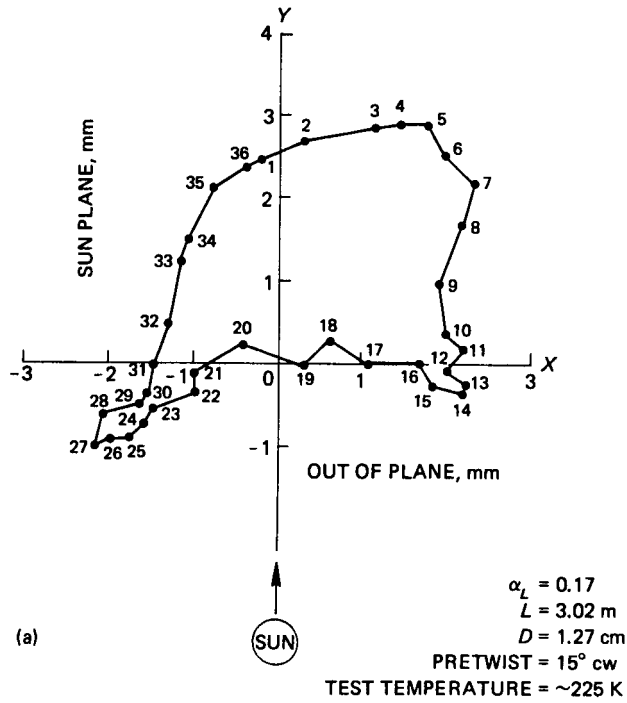


Figure 22.—Al-black-coated, interlocked Westinghouse boom with 15 percent perforation and low pretwist, test boom 9. (a) Observed coordinates. (b) Sun-rotation coordinates.

magnitude. The marked difference in thermal bending response of this boom compared to the previous one suggests that profile shape is relatively sensitive to the degree of seam spiraling, with an added contribution from the shadowing effect of the low-transparency seam.

#### **Al-Black-Coated, Perforated, Interlocked Riveted Seam (Westinghouse)**

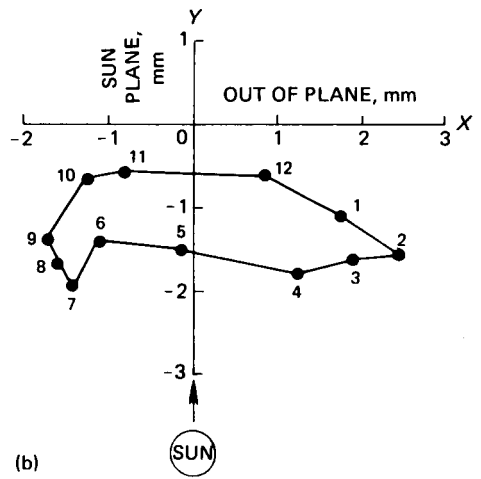
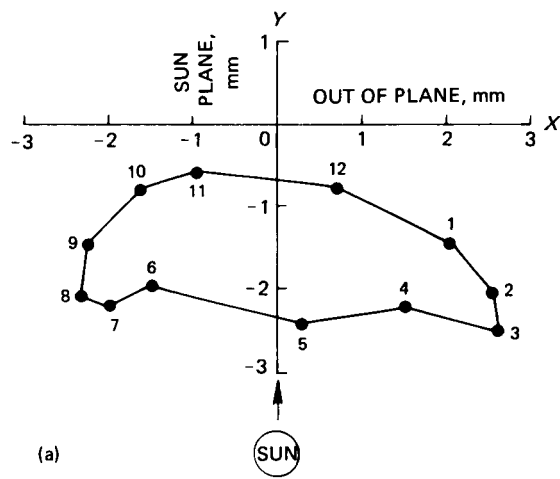
It was speculated that interlocking seams may be prone to slippage during thermal static bending. To test this hypothesis, the seam of another boom similar to the one just discussed was securely riveted at 15-cm (6-in.) intervals. The thermal bending profiles were measured at 210 and 320 K ( $-85^{\circ}$  and  $120^{\circ}$  F) and are presented in figure 23. Examination of figures 23(a) and (b) indicates that test temperature has little, if any, effect on the shape of the thermal static bending response for this concept. However, it is evident from figure 23(c) that the magnitude of static bending is reduced at the higher temperature. This behavior is consistent for all boom concepts in that thermal conductivity increases with increasing temperature, resulting in a diminished thermal gradient, the primary factor responsible for thermal bending. The most important aspect of this pattern is that it was characterized by negative Sun-plane bending. That is, the boomtip bent toward the heat source, instead of away as in the case of unperforated boom configurations. This response was not unexpected, because the perforation factor became sufficiently important in this case, as indicated by equation (4), relative to the solar-simulator absorptivity of aluminum. The Sun-plane bending vector was more positive for Sun position 12 than for position 5 because of seam shadowing. The maximum out-of-plane bending resulted again from the seam direction at Sun positions 3 and 8.

#### **Ag-Black-Coated, Perforated, Interlocked (Fairchild-Hiller)**

The RAE A satellite successfully employed 8 percent perforated Be-Cu booms of 1.42-cm (0.56-in.) diameter (ref. 8). The thermal bending response for this concept is presented in figure 24. A relatively large Sun-plane bending component is noted for most orientations of the source. In addition, it is observed that thermal bending response is essentially negative; that is, the boom bends toward the source. These experimental results confirm theoretical predictions based on an element whose surface is 8 percent perforated and which exhibits 0.04 solar-simulator absorptivity. Under actual service environment with a solar absorptivity of about 0.11, it appears that the boom would tend to a slightly positive displacement. Preliminary results of the RAE A spacecraft confirm this boom behavior, neglecting the contribution of solar pressure that pushes the boom away from the Sun approximately  $15'$ . The complex nature of the results in figure 24(a) is attributed to seam shading and reduced thermal conductance of the boom structure.

#### **Ag-Black-Coated, Perforated, Interlocked BI-STEM (SPAR)**

The initial attempt to develop a boom concept exhibiting essentially zero thermal bending consisted of a Ag-plated Be-Cu element with a black interior and incorporating both an interlocking seam and 14 percent perforations. Figures 25(a), (b), and (c) describe graphically the thermal profile of such a structure, reflecting a solar-simulator absorptivity of 0.20 for two different test temperatures. The thermal bending characteristics are similar for both temperatures, although the magnitude of the bending vector is reduced at the higher test temperature of 335 K ( $140^{\circ}$  F) because of the increase in thermal conductivity of the Be-Cu alloy. It is also evident that despite the 14-percent-perforated



$\alpha_L = 0.13$   
 $L = 3.02 \text{ m}$   
 $D = 1.27 \text{ cm}$   
 PRETWIST =  $110^\circ \text{ cw}$

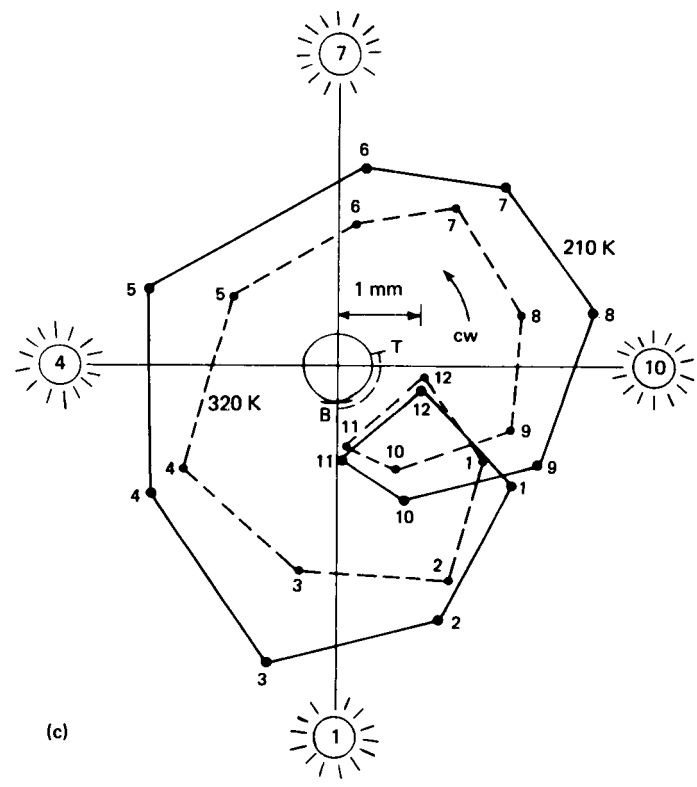


Figure 23.—Al-black-coated, interlocked, riveted-seam Westinghouse boom with 15 percent perforation, test boom 10. (a) Observed coordinates, 210 K. (b) Observed coordinates, 320 K. (c) Sun-rotation coordinates.

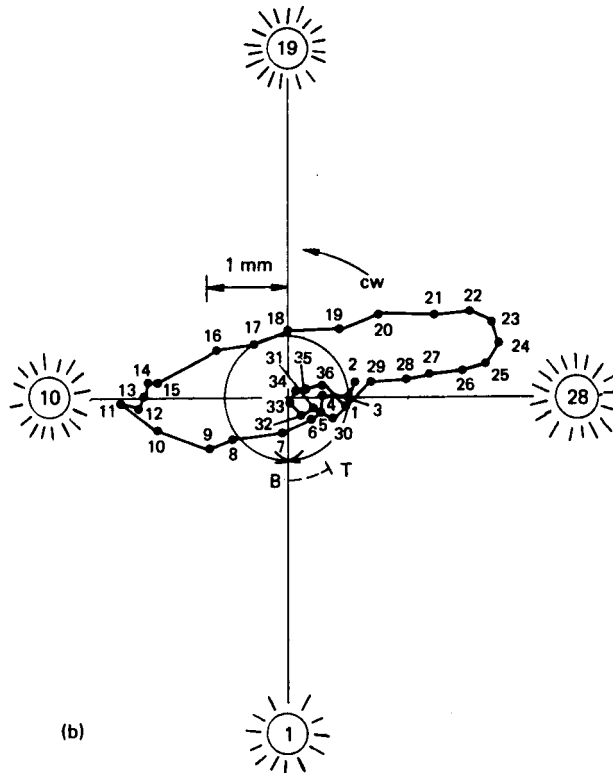
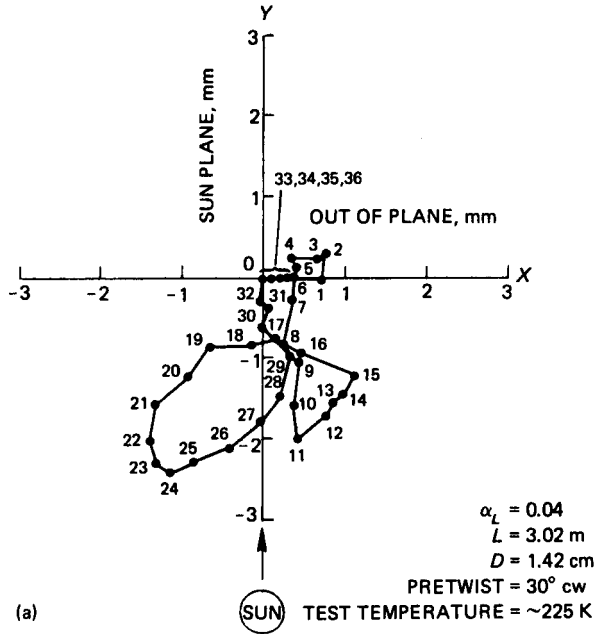
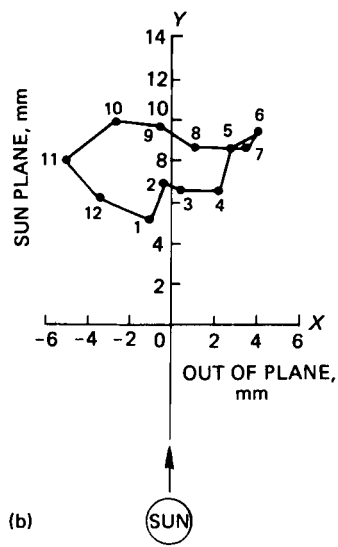
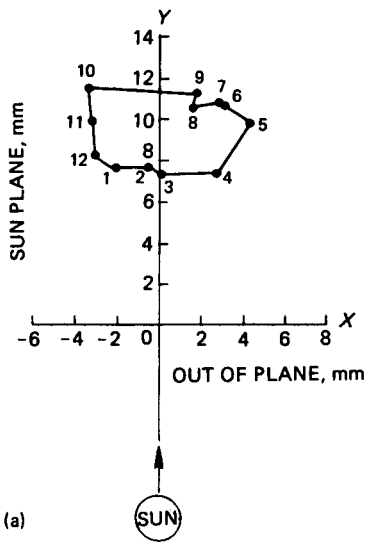


Figure 24.—Ag-black-coated, interlocked Fairchild-Hiller boom with 8 percent perforation, test boom 11. (a) Observed coordinates. (b) Sun rotation coordinates.



$\alpha_L = 0.20$   
 $L = 3.02 \text{ m}$   
 $D = 1.32 \text{ cm}$   
 PRETWIST =  $165^\circ \text{ ccw}$

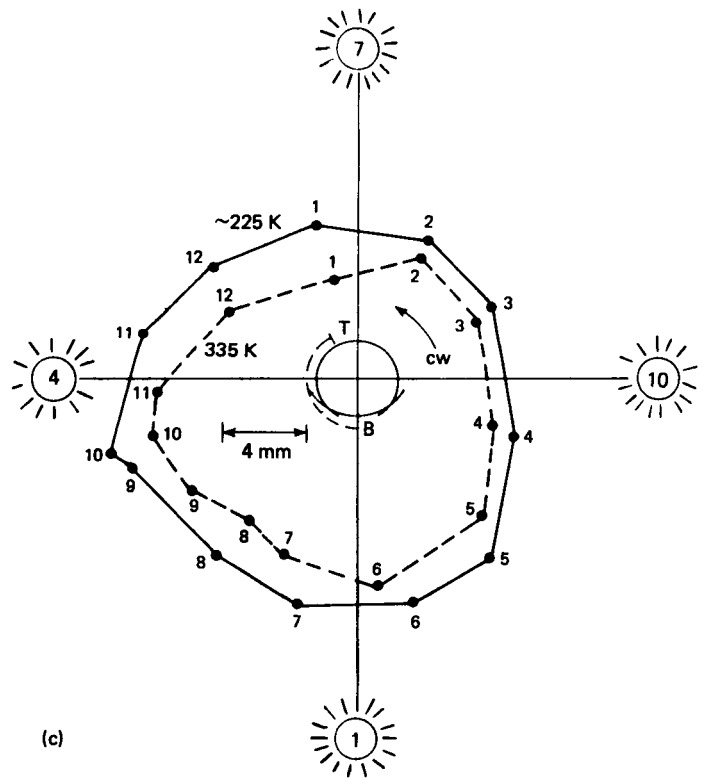
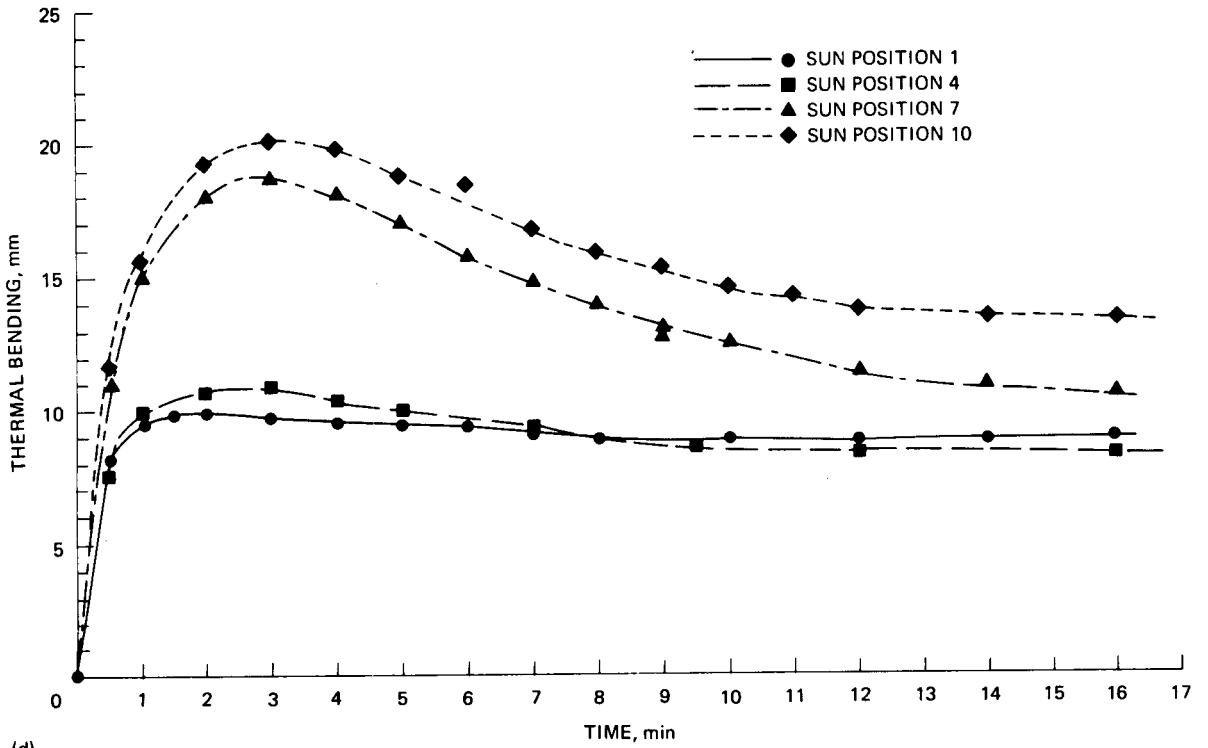
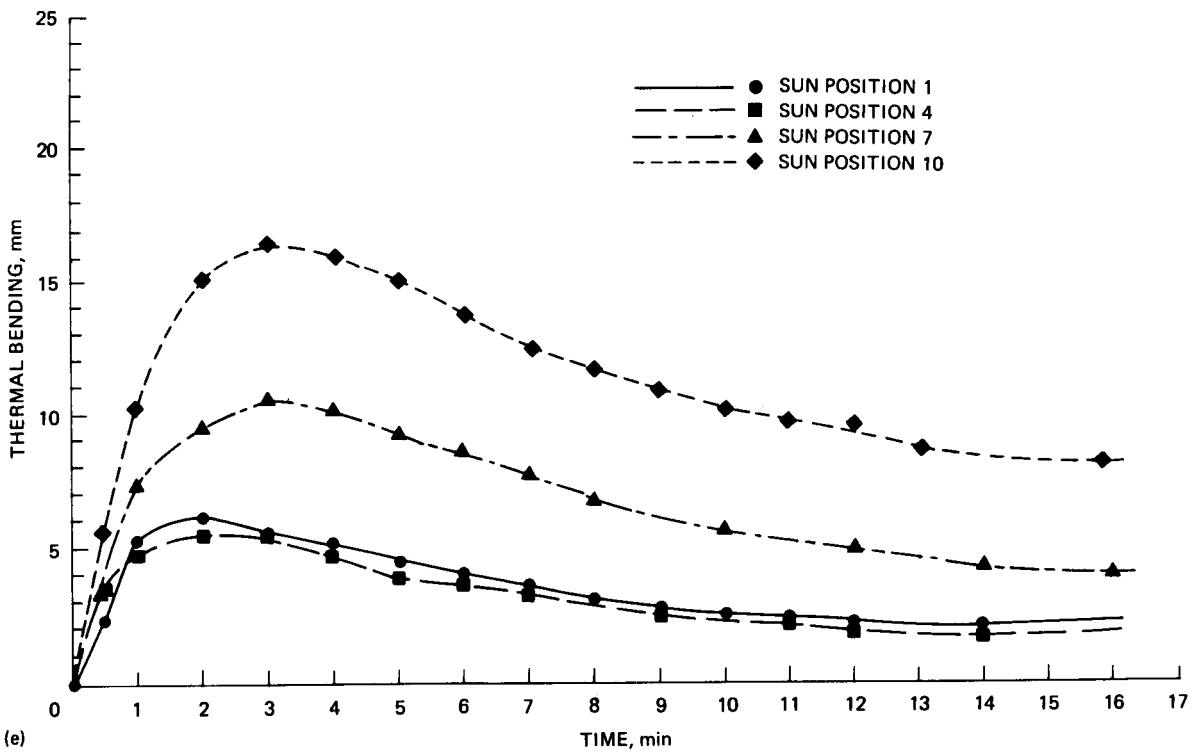


Figure 25.—Ag-black-coated, interlocked SPAR BI-STEM boom with 14 percent perforation, test boom 12. (a) Observed coordinates, 225 K. (b) Observed coordinates, 335 K. (c) Sun-rotation coordinates.



(d)



(e)

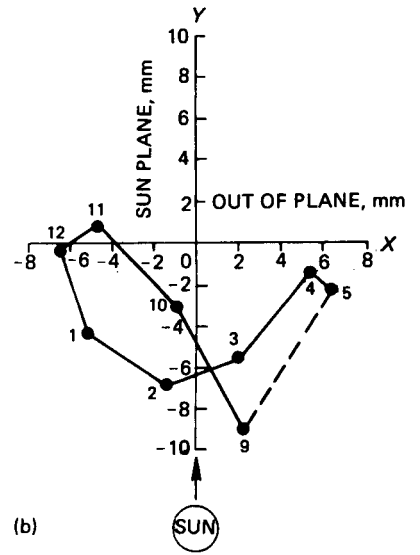
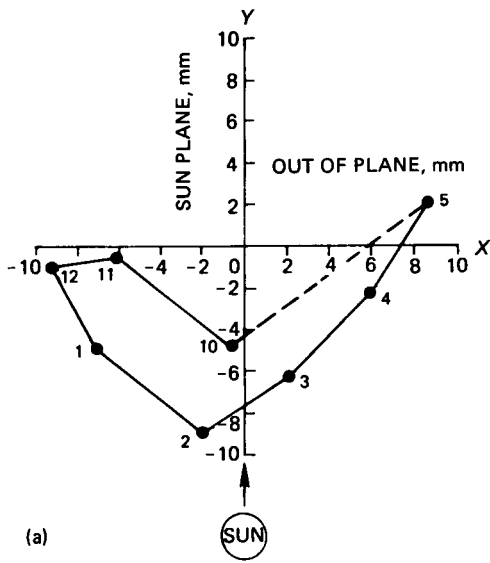
Figure 25 (continued).—(d) Sun-plane transient bending. (e) Out-of-plane transient bending.

surface, the boom exhibits significant positive Sun-plane bending because of its relatively high solar absorptivity. This suggests that the contribution of holes is not nearly as important in reducing thermal bending as the optical properties of the boom surfaces.

Figures 25(d) and (e) illustrate the relationship between thermal bending and time after the source was switched on for Sun-plane and out-of-plane bending. The curves for both bending vectors show similar trends with time, irrespective of Sun position. For Sun-position curves 1 and 4, peak bending occurs within 3 min, while for curves 7 and 10, the maxima occur within approximately 2 min. However, the magnitude of the bending vectors is significantly lower for the out-of-plane bending than for the Sun-plane bending values obtained. This is explained partly by the beneficial effects of the 165° ccw pretwist, which tends to homogenize the temperature distribution, thus promoting a more symmetrical thermal pattern indicated by the results of figure 25(c). The variation of thermal static bending with time and mean boom temperature results from nonuniform emissivity about the perimeter caused by the interlocking seam and also by the thermal time constant for radiation heat transfer associated with a given structure. Such behavior is typical of boom concepts of open cross section. The boom will experience variations in temperature gradients until thermal equilibrium conditions are established.

Subsequent efforts to further reduce thermal static bending involved application of a black coating on the interior of the BI-STEM elements and incorporating 10-, 14-, and 25-percent perforations. The solar-simulator absorptivities of the 10- and 14-percent-perforated elements, which are also significantly shorter in length, were within 5 percent of that of the previously discussed boom, while the 25-percent-perforated sample exhibited a markedly improved optical surface of  $\alpha_L = 0.08$ . In addition, the amount of pretwist incorporated in these three test booms was considerably less. The static bending values for the 25-, 14-, and 10-percent-perforated samples are shown in figures 26, 27, and 28, respectively.

The thermal profiles of all three samples, although complex, have a common characteristic; they exhibit varying degrees of negative Sun-plane bending in contrast to the positive bending displayed by the previous boom. The dominant tendency of these booms to bend in the direction of the seam because of conductance and shading effects is another similarity in thermal response for this interlocked BI-STEM concept. It is readily evident that the magnitude of negative Sun-plane bending decreases with decrease in percentage of perforations, as predicted by equation (4). Phenomenologically, as the percentage of open-hole area is reduced, there is a consequent increase in the heat absorbed on the front side of the boom relative to the back. This in turn results in an increase in thermal expansion in direct competition with the back side, which favors a more positive displacement of the element; that is, bending away from the source. The nonsymmetrical nature of the three thermal profiles probably results from the reduced pretwist and the influence of the cold seam, both of which directly influence heat conduction around the perimeter in a manner to promote heterogeneous thermal-expansion effects on either side of the boom, causing the observed large out-of-plane bending. It is debatable whether the 4-percent difference in perforation (figs. 27 and 28) played a significant role in Sun-plane bending. However, comparison between figures 25 and 26 does suggest that the substantial increase in perforated area was significant, but this view must not neglect the important contribution of the markedly improved absorptivity of the element in figure 26. This improvement changes drastically the internal-to-external-absorptivity ratio, which is the principal factor influencing degree of bending for a given structure.



$\alpha_L = 0.08$   
 $L = 2.06 \text{ m}$   
 $D = 1.27 \text{ cm}$   
 PRETWIST =  $113^\circ$  ccw

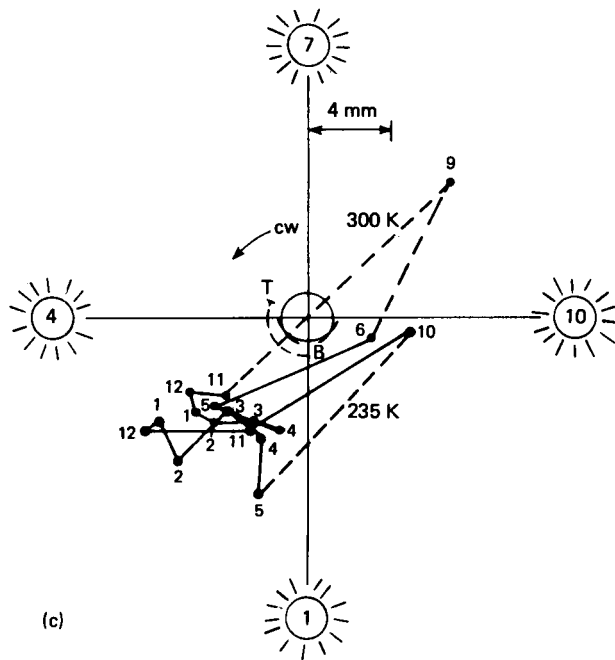


Figure 26.—Ag-black-coated, interlocked SPAR BI-STEM boom with 25 percent perforation and less pretwist, test boom 13. (a) Observed coordinates, 235 K. (b) Observed coordinates, 300 K. (c) Sun-rotation coordinates.

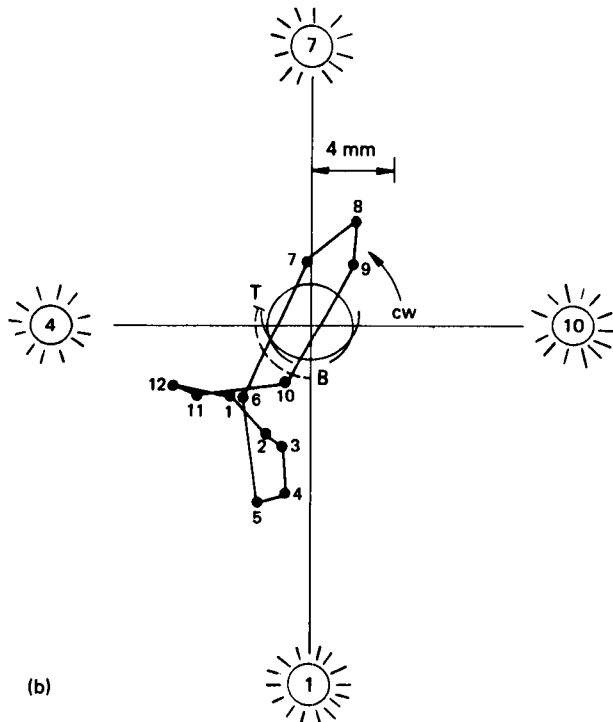
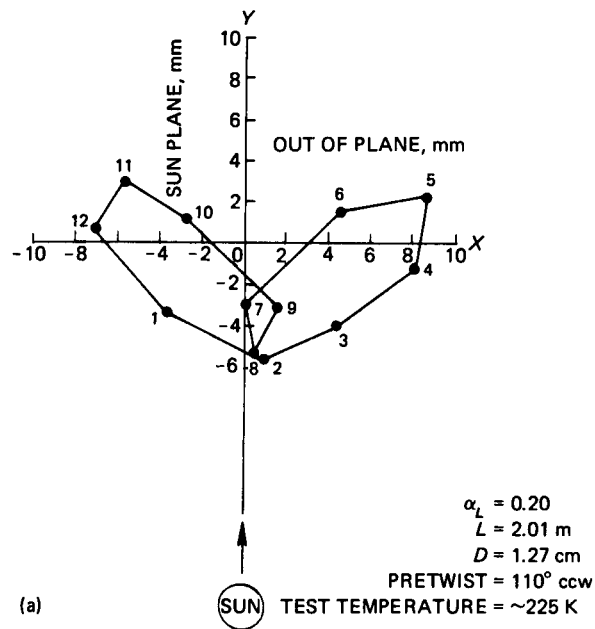
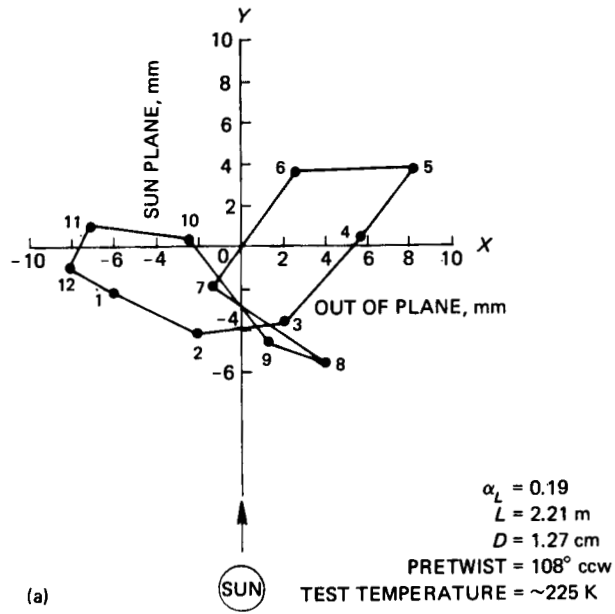
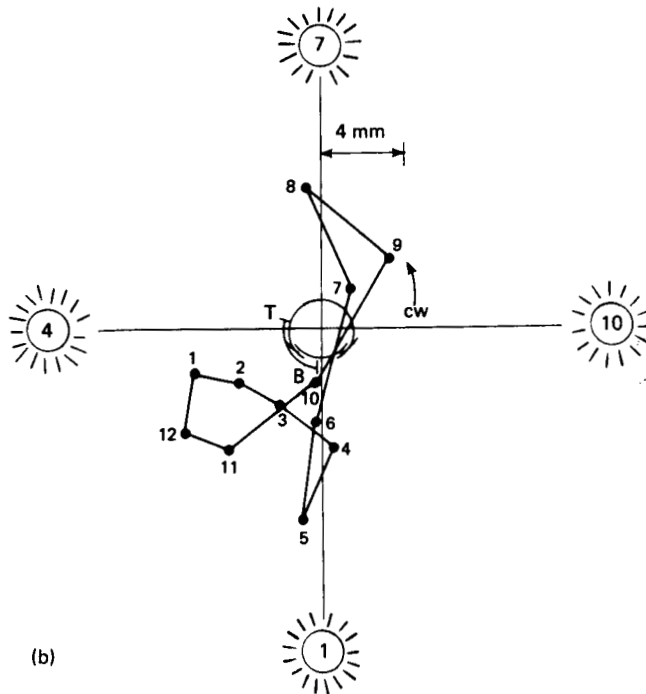


Figure 27.—Ag-black-coated, interlocked SPAR BI-STEM boom with 14 percent perforation and less pretwist, test boom 14. (a) Observed coordinates. (b) Sun-rotation coordinates.



(a)



(b)

Figure 28.—Ag-black-coated, interlocked SPAR BI-STEM boom with 10 percent perforation and less pretwist, test boom 15. (a) Observed coordinates. (b) Sun-rotation coordinates.

## Overlapped, Rigidized Wire Screen (General Dynamics/Convair)

This unique concept (ref. 9) represents a boom fabricated from dissimilar wires by conventional boom practice and subsequently rigidized at the nodes by a brazing operation. Elgiloy<sup>2</sup> (cobalt-based alloy) was used in the longitudinal direction and Be-Cu was used in the circumferential direction. The thermal static bending profiles for this boom configuration are plotted in figure 29. The dominant features of this concept are that the out-of-plane bending components are about one-half those recorded for Sun-plane bending and are relatively symmetric, as noted in figure 29(b). While this is considered an overlapped boom, the ends of the circumferential wires do interlock with the mesh to some extent and thus improve torsional rigidity. Despite the fact that the boom has 75 percent perforation, or open area, this is insufficient by itself to significantly reduce its thermal bending propensity, as equation (4) indicates. Only by the application of suitable thermal coatings can the Sun-plane vector be substantially reduced. Thus, the thermal response of this wire-screen boom further supports the contention that the perforation factor alone may not contribute significantly to improved performance.

Maximum bending occurs at Sun positions 11 and 34, at which seam orientation reduces the heat conduction around one side of the tubular element, resulting in increased temperature gradient and thermal bending. In contrast, bending is at a minimum at positions 5 and 20, because at these locations seam interference with circumferential heat conduction is negligible and temperature gradient is diminished. The reasonably symmetrical nature of the bending profile observed in figure 29(b) is ascribed to uniformity of thermal stressing due principally to the large percentage of open area of the mesh. In turn, this results not only in reduced thermal distortion in the boom along its length but in reduced thermal static twist as well.

## THERMAL STATIC BENDING AND EFFECTIVE TEMPERATURE GRADIENT

Static bending properties of deployable booms are predicted by assuming that the thin-walled cylinder of open cross section behaves like a seamless tube. However, this approach suffers from the fact that the contributions of both out-of-plane bending and thermally induced twist are neglected. In addition, inaccuracies in prediction of Sun-plane bending magnitude can occur if such factors as conduction across the seam, variation in thermal conductivity and expansion, and disparities between measured absorptivity and the actual average absorptivity of the boom are not considered in the ultimate analysis. Thus, it is evident that only by coupling experimentally derived thermal-mechanical behavior with theory can a satisfactory approximation of thermal bending response be achieved for a given boom design.

The thermal bending properties of 16 interlocked-boom concepts and two seamless-tube samples are summarized in table A-2 for comparison. Data for average Sun-plane bending and maximum static bending represent the thermal profiles shown in figures 14 to 29. The same data corrected for gravity straightening by means of equation (7) are also presented. The theoretical bending properties of a seamless tube under zero gravity were computed by using the boom physical constants with equation (3). Effective thermal gradients were calculated from the measured thermal bending data, corrected for gravity effect by use of

---

<sup>2</sup>A product of Elgin National Watch Co., Elgin, Ill.

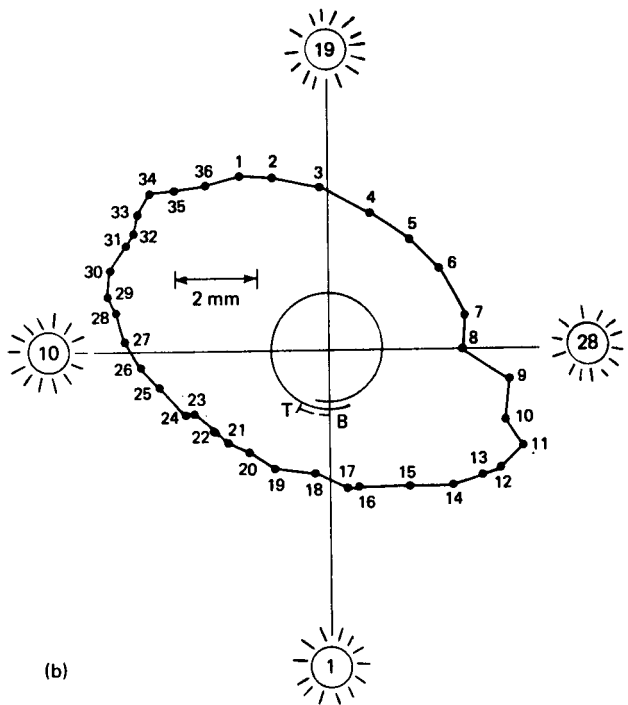
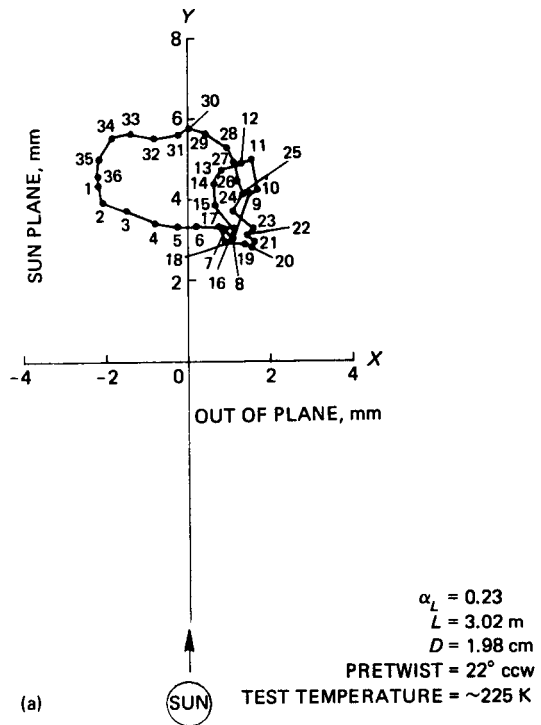


Figure 29.—Overlapped General Dynamics/Convair rigidized wire-screen boom with 75 percent perforation, test boom 16. (a) Observed coordinates. (b) Sun-rotation coordinates.

equation (7). The solar-simulator data were normalized for the solar spectrum by means of the following formula:

$$\text{Effective solar thermal gradient} = \text{effective solar-simulator thermal gradient} \times \frac{\text{solar absorptivity}}{\text{solar-simulator absorptivity}} \quad (8)$$

The absorptivity parameter  $\alpha_s/\alpha_L$  can be useful in computing the maximum thermal static bending expected for the interlocked, perforated boom design and it is necessary for the approximate scaling of thermal static bending in space. However, these values should not be confused with direct temperature-gradient measurements obtained experimentally.

As indicated earlier, certain inaccuracies result from utilizing seamless-tube theory to predict thermal static bending. However, by incorporating experimentally determined physical and mechanical properties, these discrepancies can be reduced to acceptable levels. For example, by knowing the mechanical properties and metallurgical condition of the black Be-Cu 25 alloy, a corresponding electrical conductivity of 17 percent (International Annealed Copper Standard) (ref. 6) is obtained by means of the Wiedemann-Franz law:

$$\frac{k}{\sigma T} = L$$

where

$k$  = thermal conductivity,  $\text{W m}^{-1} \text{K}^{-1}$

$\sigma$  = electrical conductivity,  $\Omega^{-1} \text{m}^{-1}$

$T$  = absolute temperature, K

$L$  = Lorentz constant,  $2.45 \times 10^{-8} \Omega \text{W K}^{-2}$

The thermal conductivity of this boom material is calculated to be  $67 \text{ W m}^{-1} \text{K}^{-1}$  at 296 K ( $39 \text{ Btu}/(\text{hr } ^\circ\text{F ft})$  at  $72^\circ \text{F}$ ). With this information, the Sun-plane thermal bending of the black seamless tube is computed to be 3.30 cm (1.30 in.) compared to a measured value of 2.93 cm (1.15 in.), corrected for measurement temperature. Subtracting the 4-percent error attendant with the seamless-tube formula from the observed difference of 13 percent between measured and computed bending values leads to a final corrected error of only 9 percent. This good agreement provides the means for calibrating the test facility, using the black-coated seamless tube.

In contrast, the thermal bending calculated for the uncoated Be-Cu seamless tube using the same thermal conductivity constant is 1.00 cm (0.395 in.) compared to a measured value of 0.48 cm (0.19 in.). This observed error of about 100 percent is explained by the fact that small differences in reflectivity  $R$  involving samples of  $1.6\text{-cm}^2$  ( $0.25\text{-in}^2$ ) area are compared to large variations in optical properties associated with the  $970\text{-cm}^2$  ( $150\text{-in}^2$ ) boom surface areas. This leads to significant changes in absorptivity ( $\alpha = 1 - R$ ) that may lead to marked inaccuracy of the calculated bending value. The accuracy of the absorptance measurement is within +1 percent. It is not surprising in some instances to find 100 percent variations in measured  $\alpha_s$  from selected samples taken along the full length of a boom that visually appears to be optically uniform. This source of error was further supported by comparing the magnitudes of measured thermal bending with calculated values of several Be-Cu and

stainless steel seamless tubes that were 0.13 mm (0.005 in.) thick and 1.3 cm (0.50 in.) in diameter. These results indicated a variation in thermal bending ranging from 40 to 70 percent of the calculated value. It is evident that the good agreement in results with the black-coated boom must be attributed to its high absorptivity, which is relatively insensitive to small sampling variations over the entire length of the boom. As indicated above, absorptivity values calculated from absorption-versus-wavelength curves representing several Be-Cu samples removed from a 3.0-m (10-ft) boom varied by as much as 100 percent. However, it is interesting to note that the ratio of solar absorptivity to solar-simulator absorptivity  $\alpha_S/\alpha_L$  for each sample tested remained essentially invariant when  $\alpha_S$  and  $\alpha_L$  varied. Therefore, scaling the temperature gradient from the solar-simulator spectrum to the solar spectrum using the  $\alpha_S/\alpha_L$  factor (eq. (8)) does not introduce a significant error in the computation.

The thermal bending results presented in table A-2 permit a comparison to be made between experiment and prediction by seamless-tube theory. It is evident that the degree of agreement achieved between theory and experiment is dependent upon the structural concept considered as well as the thermal-control coatings that are applied to the boom surface. For example, the ratios of measured Sun-plane bending to calculated values for three single-interlocking Be-Cu booms (boom 1, 1.27 cm (0.50 in.); boom 4, 2.30 cm (0.91 in.); and boom 2, 1.5 cm (0.58 in.) Ag-plated) are 0.41, 0.45, and 0.47, respectively. This ratio compares favorably with that of 0.48 obtained from the bare Be-Cu seamless tube. On the other hand, a similar comparison of three Ag-plated, dual-interlocking-seam concepts (such as boom 3, 1.27 cm (0.50 in.) Hingelock; boom 5, 1.27 cm (0.50 in.) SPAR BI-STEM; and boom 6, 0.71 cm (0.28 in.) SPAR BI-STEM—reveals significantly larger Sun-plane bending ratios of 0.74, 1.24, and 0.97, respectively. This discrepancy can be explained by noting that the existence of an additional interlocking seam provides a further barrier to heat conduction from front to back resulting in an increased thermal gradient and consequent bending. It is interesting to note that these ratios agree reasonably well with the ratio (0.87) of a Be-Cu seamless tube that was deliberately painted black on the outside to induce greater thermal bending. This is not to suggest, however, that the effect of such an optical surface is equivalent to the introduction of a mechanical seam in terms of thermal bending properties for a given boom configuration.

The thermal bending performance of several perforated booms is also presented in table A-2. For a given percentage of open-hole area, the benefit of introducing only a highly reflective external coating appears questionable, as indicated by the data obtained on a 15-percent-perforated, interlocked Be-Cu Westinghouse boom and a 14-percent-perforated, Ag-plated, SPAR BI-STEM with two interlocking seams. Their average Sun-plane bending to seamless-tube ratios for the Westinghouse and SPAR BI-STEM are 0.78 and 1.02, respectively. This suggests that the reduction in thermal conductance of the double-interlocked BI-STEM was largely responsible for the increase in thermal static bending, thus offsetting the benefits of a highly reflective Ag-plated external surface.

The calculated thermal static bending value in the Sun plane for the rigidized wire-screen boom is very close to that determined experimentally, that is, the bending ratio is 1.07. The calculated magnitude of static bending was arrived at by obtaining the temperature gradient from a heat transfer model by Howell (ref. 10) and employing appropriate values of  $\alpha_L$  and thermal conductivity, along with equation (7). Even the shape of the bending curve predicted by Howell's model agrees with the thermal profile derived experimentally (fig. 29(a)). It is important to note that despite the high percentage of open area, the wire-grid concept suffers significant bending and thus requires the use of thermal coatings for optimum performance.

With the application of appropriate thermal coatings, as in the case of the three 15-percent-perforated aluminum-black Westinghouse booms and the 8-percent-perforated Ag-black Fairchild-Hiller boom, the magnitude of observed thermal static bending dropped considerably, as indicated in the tabular results. Whereas the measured values have the same sign as those calculated, the numerical agreement suffers from the fact that at very small tip displacements, the seam (neglected in eq. (4)) assumes a more controlling role in bending propensity. The effective solar temperature gradient for the RAE design (boom 11) was measured to be 0.28 K (0.50° F), which compares favorably with the value of 0.42 K (0.75° F) obtained from service performance on the RAE A spacecraft.<sup>3</sup>

When they combine the beneficial effects of seam interlocking, perforation, and optimum thermal coating on external and internal surfaces, the Westinghouse and Fairchild-Hiller concepts develop a relative small, positive, effective-temperature gradient (nominally 0.3 K (0.5 F°)). Consequently, the low value of thermal static bending (Sun-plane component) observed is as predicted, and for a 3.0-m (10-ft) boom element the magnitude of tip deflection is less than 0.4 cm (0.16 in.).

In the development of the SPAR concept of a Ag-plated, black interior, interlocked BI-STEM, three different amounts of perforated surface area were examined: 10, 14, and 25 percent. The thermal bending data and calculated values reported were scaled to 3.0-m (10-ft) length using equations (4) and (6). The average negative Sun-plane bending was observed to decrease as the perforated area decreased. The agreement of the sign of the average Sun-plane bending observed with that calculated for a perforated seamless tube was inconsistent. This discrepancy is attributed to the influence of the double seam and the overlapping effect of the inner and outer elements inherent in the BI-STEM design. For the 10- and 14-percent-perforated BI-STEM designs, the effective solar thermal gradients were essentially the same as reported for the previously discussed Westinghouse and Fairchild-Hiller boom configurations. However, the magnitude of maximum thermal bending for the BI-STEM configuration was significantly larger than either of the other two. Enhancement of the optical properties of the BI-STEM surface coating together with enlarged perforated hole patterns along the edges of the inner element should reduce the level of thermal static bending observed.

## CONCLUSIONS

The design and development of the thermal-mechanical test facility along with experimental techniques to measure thermal static distortion provide part of the technology necessary for experimental evaluation of potentially promising deployable-boom structures for spacecraft application.

The measured values of average Sun-plane and maximum thermal static bending values for 16 interlocked booms were found to be within a factor of 2.5 of the thermal bending values predicted by analysis based on seamless or perforated seamless tubes.

The test facility permits out-of-plane bending profiles to be measured for interlocked booms; these are not predicted by seamless-tube analysis. However, a complex thermal-distortion analysis has been devised to predict out-of-plane bending properties of an overlapped wire-grid boom and has been confirmed by experiment.

---

<sup>3</sup>J. Fedor: Private communication, Apr. 1971.

The effective solar thermal gradients determined from these investigations in conjunction with seamless-tube analysis can be used to predict thermal static bending.

The development of a torsionally stiff, zero-thermal-gradient BI-STEM boom was advanced by the thermal-distortion measurements obtained on test samples during the development stage of fabrication.

#### **ACKNOWLEDGMENTS**

The authors wish to thank Robert Simms for the many hours of tedious measurements as well as for designing and installing much of the electronic measurement and control systems. The authors are grateful for the discussions and analysis of boom thermal mechanics with Harold Frisch, Henry Price, and Henry Hoffman. Thanks go to Dr. Matthew Thekaekara for calibrating the radiometer and solar simulator, to Dr. Paul Lillienthal for calculating the gravity-induced boom bending, and to Norm Ackerman for the heat transfer calculations. The authors appreciate the aid of Henry Sweet and James Jarrett in the development and calibration of the test chamber.

**Appendix**

**TEST BOOM PROPERTIES, BENDING MEASUREMENTS,  
AND ABSORPTIVITIES**

Table A-1.—Test Boom Properties

Test boom number and design	Manufacturer	Diameter, cm	Length, m	Thermal conductivity, $W m^{-1} K^{-1}$	Thickness, mm	Straightness, <sup>a</sup> mm	Solar absorptivity $\alpha_S$	Solar-simulator absorptivity $\alpha_L$	Mass length, $mg m^{-1}$
Seamless tubes:									
Black Be-Cu	—	1.27	3.02	69	0.140	—	0.95	0.95	45.8
Be-Cu	—	1.27	3.02	52	.145	34.5	.38	.22	45.8
Interlocked:									
(1) Be-Cu	Westinghouse	1.27	3.02	50	.053	19.6	.46	.19	18.8
(2) Ag-plated Be-Cu	Fairchild-Hiller	1.47	3.02	67	.056	15.7	.10	.04	20.9
(3) Ag-plated Be-Cu Hingelock	Fairchild-Hiller	1.27	3.02	76	.061	29.5	.15	.05	25.8
(4) Be-Cu	Fairchild-Hiller	2.30	3.02	104	.102	30.2	.37	.18	70.8
(5) Ag-plated Be-Cu BI-STEM	SPAR Aerospace	1.30	3.02	102	.053	21.3	.13	.05	22.0
(6) Ag-plated Be-Cu BI-STEM	SPAR Aerospace	.71	3.02	95	.036	7.1	.20	.07	9.1
				b <sub>119</sub>					
Perforated interlocked:									
(7) Be-Cu	Westinghouse	1.27	3.02	55	.056	13.7	.44	.15	15.6
(8) Al-black-coated	Westinghouse	1.27	3.02	55	.051	12.2	.27	.19	14.7
(9) Al-black-coated, low pretwist	Westinghouse	1.27	3.02	55	.053	12.7	.23	.17	15.2
(10) Al-black-coated, riveted	Westinghouse	1.27	3.02	52	.053	18.3	.20	.13	15.2
				b <sub>73</sub>					
(11) Ag-black-coated	Fairchild-Hiller	1.42	3.02	67	.056	45.0	c <sub>.11</sub>	c <sub>.04</sub>	19.5
(12) Ag-black-coated, 14 percent perforated BI-STEM	SPAR Aerospace	1.32	3.02	102	.056	26.7	.33	.20	19.1
				b <sub>123</sub>					
(13) Ag-black-coated, 25 percent perforated BI-STEM	SPAR Aerospace	1.27	2.06	69	.048	36.8	.16	.08	18.2
(14) Ag-black-coated, 14 percent perforated BI-STEM	SPAR Aerospace	1.27	2.01	69	.051	6.6	.32	.20	18.9
(15) Ag-black-coated, 10 percent perforated BI-STEM	SPAR Aerospace	1.27	2.21	69	.051	19.3	.29	.19	18.9
(16) Wire grid, 75 percent perforated, overlapped	General Dynamics/Convair	1.98	3.02	93	—	24.1	.36	.23	20.8

<sup>a</sup>Tip displacement due to manufacturing tolerances.

<sup>b</sup>The greater thermal-conductivity values were measured at higher test temperatures (table A-2).

<sup>c</sup>Absorptivity values were taken from booms flown on RAE A spacecraft.

Table A-2.—Thermal Bending and Effective Thermal Gradients

Test boom number and design	Manufacturer	Test temperature, K	Thermal bending, mm				Seamless-tube theory	Effective thermal gradient, K			
			Measured		Zero gravity			Solar simulator		Solar	
			Average Sun plane	Maximum	Average Sun plane	Maximum		Average Sun plane	Maximum		
Seamless tubes: Black Be-Cu Be-Cu	— —	300 215	25.8 4.2	— —	29.3 4.8	— —	33.0 10.0	4.86 .80	— —	4.88 1.36	— —
Interlocked: (1) Be-Cu (2) Ag-plated Be-Cu (3) Ag-plated Be-Cu Hingelock (4) Be-Cu (5) Ag-plated Be-Cu BI-STEM (6) Ag-plated Be-Cu BI-STEM	Westinghouse Fairchild-Hiller Fairchild-Hiller Fairchild-Hiller SPAR Aerospace SPAR Aerospace	~225 ~225 270 365 ~225 195 315	8.6 1.6 2.3 4.6 3.6 2.7 2.3	9.9 2.4 2.9 5.6 4.2 3.5 2.9	9.9 2.0 2.7 4.7 4.0 3.9 3.3	11.2 2.8 3.4 5.8 4.7 5.1 4.2	25.1 4.2 3.7 10.5 3.3 4.1 3.2	1.6 .34 4.6 1.39 .68 .37 .31	1.8 .53 5.7 1.71 .78 .48 .40	3.9 .88 1.38 2.90 1.70 1.02 .85	4.3 1.34 1.63 3.55 1.95 1.33 1.10
Perforated interlocked: (7) Be-Cu (8) Al-black-coated (9) Al-black-coated, low pretwist (10) Al-black-coated, riveted	Westinghouse Westinghouse Westinghouse Westinghouse	~225 ~225 ~225 320	8.0 .7 -1.7 -1.3	9.0 3.3 3.4 -3.6	9.6 .8 .8 -2.0	10.7 3.9 4.0 -4.2	12.3 5.4 3.6 -8	1.59 .14 .10 -.34	1.76 .63 .75 .71	4.62 .36 .23 .28	5.12 1.63 1.81 —
(11) Ag-black-coated (12) Ag-black-coated, 14 percent perforated BI-STEM (13) Ag-black-coated, 25 percent perforated BI-STEM (14) Ag-black-coated, 14 percent perforated BI-STEM (15) Ag-black-coated, 10 percent perforated BI-STEM (16) Wire grid, 75 percent perforated, overlapped	Fairchild-Hiller SPAR Aerospace SPAR Aerospace SPAR Aerospace SPAR Aerospace General Dynamics/Convair	~225 335 235 300 ~225 ~225	-9 7.7 -6.2 -6.9 -3.1	-2.6 12.1 9.1 -17.7 -18.3 -12.8	-1.0 11.0 8.8 -6.6 -7.4 -3.2	-2.9 13.8 10.4 -18.8 -19.4 -13.3	-2.8 10.8 9.0 -7.5 — 7.0	-.20 1.92 1.53 -1.09 -1.21 -.53	-.55 2.40 1.81 -3.12 -3.22 -2.20	-.28 2.72 2.18 -.46 -.51 .37	— 3.41 2.57 — — —
		~225	-2.5	-10.5	-2.6	-11.0	9.3	-.43	-1.71	.0	—
		~225	4.2	5.8	4.8	6.6	4.4	1.37	1.91	2.08	2.91

Table A-3.—Solar Absorptivity for Be-Cu Seamless Tubes

Wavelength, nm		Solar flux $J_S$ , $mW\ cm^{-2}$	Reflectance from spectra $R$	Reflectance for aluminum $R_{Al}$	$RR_{Al}$	Absorptivity $1 - RR_{Al}$	Spectral absorptivity, $mW\ cm^{-2}$
Range	Weighted average						
220 to 240	230	0.1001	0.094	0.917	0.086	0.914	0.091
240 to 260	250	.1574	.091	.921	.084	.916	.144
260 to 280	270	.4434	.088	.922	.081	.919	.407
280 to 300	290	1.0298	.088	.923	.081	.919	.946
300 to 320	310	1.4732	.091	.924	.084	.916	1.349
320 to 340	330	2.2026	.100	.924	.092	.908	1.999
340 to 360	350	2.3885	.113	.925	.105	.895	2.139
360 to 380	370	2.6030	.128	.925	.118	.882	2.295
380 to 400	390	2.4886	.156	.924	.144	.856	2.130
400 to 420	410	3.8185	.178	.923	.164	.836	2.659
420 to 440	430	3.8614	.212	.923	.196	.804	3.106
440 to 460	450	4.4337	.227	.922	.209	.791	3.506
460 to 480	470	4.4337	.258	.920	.237	.763	3.382
480 to 500	490	4.1475	.287	.920	.264	.736	3.053
500 to 520	510	4.0044	.319	.917	.293	.707	2.833
520 to 540	530	3.8614	.365	.917	.335	.665	2.569
540 to 560	550	4.0045	.433	.916	.397	.603	2.416
560 to 580	570	3.8614	.512	.914	.468	.532	2.055
580 to 600	590	3.8614	.567	.914	.518	.482	1.860
600 to 620	610	3.5755	.581	.907	.527	.473	1.692
620 to 640	630	3.4324	.632	.907	.573	.427	1.465
640 to 660	650	3.4324	.654	.903	.591	.409	1.406
660 to 680	670	3.1464	.677	.901	.610	.390	1.227
680 to 700	690	3.0034	.694	.901	.625	.375	1.126
700 to 720	710	2.8604	.715	.890	.636	.364	1.040
720 to 740	730	2.7174	.733	.890	.652	.348	.945
740 to 750	745	1.4302	.751	.890	.668	.332	.474
750 to 800	775	6.0068	.775	.872	.676	.324	1.947
800 to 850	825	5.4348	.802	.860	.690	.310	1.686
850 to 900	875	4.8627	.798	.874	.697	.303	1.471
900 to 950	925	4.2906	.786	.904	.711	.289	1.242
950 to 1000	975	4.0046	.782	.928	.726	.274	1.099
1000 to 1100	1050	6.8650	.784	.954	.748	.252	1.731
1100 to 1200	1150	5.5778	.792	.954	.756	.245	1.364
1200 to 1300	1250	4.7197	.800	.954	.763	.237	1.118
1300 to 1400	1350	3.7185	.808	.954	.771	.229	.852
1400 to 1500	1450	3.0034	.813	.954	.776	.224	.674
1500 to 1600	1550	2.5744	.819	.970	.794	.206	.529
1600 to 1700	1650	2.0452	.825	.970	.800	.120	.409
1700 to 1800	1750	1.7162	.830	.970	.805	.195	.334
1800 to 1900	1850	1.4159	.837	.970	.812	.188	.266
1900 to 2000	1950	1.2157	.841	.970	.816	.184	.224
2000 to 2100	2050	1.0154	.848	.974	.826	.174	.177
2100 to 2200	2150	.8867	.850	.974	.828	.172	.153
2200 to 2300	2250	.7294	.855	.974	.833	.167	.122
2300 to 2400	2350	.6722	.860	.974	.838	.162	.109
2400 to 2500	2450	.5578	.860	.974	.838	.162	.091
Total							63.912

$$\text{Solar absorptivity } \alpha_S = \frac{\sum J_S \alpha}{140} = 0.45651$$

Table A-4.—Solar-Simulator Absorptivity for Be-Cu Seamless Tubes

Wavelength, nm		Lamp flux $J_L$ , mW cm <sup>-2</sup>	Reflectance from spectra $R$	Reflectance for aluminum $R_{Al}$	$RR_{Al}$	Absorptivity $\alpha$ $1 - RR_{Al}$	Spectral absorptivity, mW cm <sup>-2</sup>
Range	Weighted average						
300 to 600	550	4.06	0.433	0.916	0.397	0.603	2.450
600 to 700	650	5.75	.654	.903	.591	.409	2.355
700 to 800	750	7.44	.753	.890	.670	.330	2.454
800 to 900	850	9.04	.800	.865	.692	.308	2.784
900 to 1000	950	10.22	.784	.915	.717	.283	2.889
1000 to 1200	1100	21.15	.788	.954	.752	.248	5.252
1200 to 1400	1300	18.79	.804	.954	.767	.233	4.378
1400 to 1600	1500	15.09	.816	.954	.778	.222	3.344
1600 to 1800	1700	12.37	.827	.970	.899	.101	1.248
1800 to 2000	1900	9.70	.839	.970	.814	.186	1.806
2000 to 2200	2100	7.50	.849	.974	.827	.173	1.298
2200 to 2500	2350	9.04	.860	.974	.838	.162	1.468
Total							31.726

$$\text{Solar-simulator absorptivity } \alpha_L = \frac{\sum J_L \alpha}{130.14} = 0.2438$$

## REFERENCES

1. Warren, H. R.; and MacNaughton, J. D.: "The Use of Extendible Booms for Space Aerials and for Satellite Attitude Control." *Int. Astronaut. Congr., Proc., 14th*, E. Brun and I. Hersey, eds., 1963, pp. 317-340.
2. Frisch, H. P.: *Coupled Thermally-Induced Transverse Plus Torsional Vibrations of a Thin-Walled Cylinder of Open Section*. NASA TR-R-333, 1970.
3. Thekaekara, M. P.: "Revised Standards for the Solar Constant and the Solar Spectrum." *Significant Accomplishments in Technology, Goddard Space Flight Center, 1970*. NASA SP-295, 1972, pp. 133-137.
4. Thekaekara, M. P.: *The Solar Constant and the Solar Spectrum Measured From a Research Aircraft*. NASA TR-R-351, 1970.
5. Kemper, A.; and Farrell, K.: *Temperature Gradients and Profile Changes in Long Tubular Elements Due to Incident Radiation*. DHC-SP-TN-164 (NRL Contract NR 3592(00)(X)), De Havilland Aircraft, Ltd., Dec. 1962.
6. Rosenberg, H. M.: *Low-Temperature Solid State Physics*, Oxford Univ. Press, 1963.
7. Drummeter, L. F., Jr.; and Hass, G.: "Solar Absorptance and Thermal Emittance of Evaporated Coatings." Vol. 2 of *Physics of Thin Films*, G. Hass and R. E. Thun, eds., Academic Press, Inc., 1964.
8. *Gravity Gradient Subsystem*. Report 826-FR-1 (NAS5-10228), Fairchild-Hiller Corp., 1970.
9. Wiant, H. R.: *Gravity Gradient Boom and Antenna Materials Study*. Report GDC-22L-67-010 (NAS5-9597), Convair Div., General Dynamics Corp., Aug. 18, 1967.
10. Howell, G. A.: *Mathematical Model and Computer Program for Solution of Temperature Around a Screen-Type Tubular Gravity Gradient Element*. (NAS5-9597), Convair Div., General Dynamics Corp., Aug. 1967.